JGR Solid Earth

RESEARCH ARTICLE
10.1029/2022JB025504

The Evolution of Pore Pressure, Stress, and Physical Properties During Sediment Accretion at Subduction Zones

M. A. Nikolinakou[1], P. B. Flemings[2,3], B. Gao[2,3], and D. M. Saffer[2,3]

[1]Bureau of Economic Geology, Jackson School of Geosciences, The University of Texas at Austin, Austin, TX, USA, [2]Department of Geological Sciences, Jackson School of Geosciences, The University of Texas at Austin, Austin, TX, USA, [3]Institute for Geophysics, Jackson School of Geosciences, The University of Texas at Austin, Austin, TX, USA

Key Points:

- Stress evolution from uniaxial to compressional state results in overpressure generation, fluid expulsion, and compaction
- Both mean and shear stress changes contribute to pressure generation; shear-induced pressures are significant at and outboard of the trench
- High overpressures result in a weakened décollement that onsets ahead of the trench and persists tens of km into the subduction zone

Correspondence to:
M. A. Nikolinakou,
mariakat@mail.utexas.edu

Citation:
Nikolinakou, M. A., Flemings, P. B., Gao, B., & Saffer, D. M. (2023). The evolution of pore pressure, stress, and physical properties during sediment accretion at subduction zones. *Journal of Geophysical Research: Solid Earth*, *128*, e2022JB025504. https://doi.org/10.1029/2022JB025504

Received 2 SEP 2022
Accepted 8 JUN 2023

Author Contributions:
Conceptualization: M. A. Nikolinakou, P. B. Flemings, D. M. Saffer
Formal analysis: M. A. Nikolinakou, B. Gao
Funding acquisition: M. A. Nikolinakou, P. B. Flemings
Investigation: M. A. Nikolinakou, B. Gao
Methodology: M. A. Nikolinakou, P. B. Flemings, B. Gao, D. M. Saffer
Project Administration: P. B. Flemings
Resources: D. M. Saffer
Supervision: M. A. Nikolinakou, P. B. Flemings, D. M. Saffer
Validation: M. A. Nikolinakou, B. Gao
Visualization: M. A. Nikolinakou, P. B. Flemings, D. M. Saffer

Abstract We study stress, pressure, and rock properties in evolving accretionary wedges using analytical formulations and geomechanical models. The evolution of the stress state from that imposed by uniaxial burial seaward of the trench to Coulomb failure within the wedge generates overpressure and drives compaction above the décollement. Changes in both mean and shear stress generate overpressure and shear-induced pressures play a particularly important role in the trench area. In the transition zone between uniaxial burial and Coulomb failure, shear-induced overpressures increase more than overburden and are higher than footwall pressures. This rapid increase in overpressure reduces the effective normal stress and weakens the plate interface along a zone that onsets ahead of the trench and persists well into the subduction zone. It also drives dewatering at the trench, which enables compaction of the hanging-wall sediments and a porosity offset at the décollement. Within the accretionary wedge, sediments are at Coulomb failure and the pore pressure response is proportional to changes in mean stress. Low permeability and high convergence rates promote overpressure generation in the wedge, which limits sediment strength. Our results may provide a hydromechanical explanation for a wide range of observed behaviors, including the development of protothrust zones, widespread occurrence of shallow slow earthquake phenomena, and the propagation of large shallow coseismic slip.

Plain Language Summary Earth's subduction zones form where two tectonic plates converge and one plate descends, or subducts, beneath the other (overriding plate). Overriding sediments are plowed onto the continent the way dirt piles up in front of a bulldozer. Some of the largest, most destructive, and tsunami-generating earthquakes are produced along plate boundaries during subduction. The sediment behavior of both plates depends on changes in fluid pressure and stress, which are caused by tectonic forces (analogous to the bulldozer push). The strength of the plate boundary—which controls earthquake mechanics—also depends on fluid pressure, stress, and sediment rock properties. We use analytical and numerical models to simulate a subduction zone's evolution through space and time. The models use sediment-behavior laws that account for the interaction between fluids and sediments, as the plates deform. We show that stress changes associated with the piling up of sediments generate abnormally high fluid pressures in the shallow parts of the subduction. These high pressures weaken the plate boundary, and limit powerful earthquakes to deeper in the crust. The stress changes also result in more compacted sediments and focused dewatering at the seafloor in the shallow areas of the subduction zone.

1. Introduction

Stress, pore pressure, and deformation are coupled in geologic systems and evolve as a function of the geologic loading history (e.g., Flemings, 2021; Gradmann & Beaumont, 2017; Hauser et al., 2014; Nikolinakou et al., 2018). These quantities impact fundamental geological processes, such as basin evolution, earthquake slip behavior, and volatile fluxes between the solid Earth and oceans. This is because sediment compaction, permeability, elastic moduli, and shear strength all depend on the state and evolution of the full stress tensor, including deviatoric stresses and the pore fluid pressure (Flemings & Saffer, 2018; Gamage et al., 2011; Scholz, 2012; Suppe, 2014; Terzaghi et al., 1996).

In subduction zones, tectonic loading increases the lateral stress in accreted sediments (Figure 1) (D. Davis et al., 1983; Hubbert & Rubey, 1959). This increase, together with increasing vertical stress due to burial, drives overpressure generation in the accreted, hanging-wall sediments. The rate of overpressure dissipation depends on the sediment permeability, compressibility, and the flow path length (e.g., Craig, 2005; Gamage et al., 2011;

Writing – original draft: M. A. Nikolinakou, P. B. Flemings, B. Gao, D. M. Saffer
Writing – review & editing: M. A. Nikolinakou, P. B. Flemings, D. M. Saffer

Neuzil, 1995), all of which evolve as the sediment is consumed in the subduction zone and deforms. For the high compressibility and low permeability sediments found commonly in growing accretionary wedges, particularly at depths <10 km, the overpressure generation outpaces the rate of pressure dissipation by drainage (Flemings & Saffer, 2018; Saffer & Tobin, 2011; Suppe, 2007). Any dissipation of overpressure, in turn, leads to an increase in effective stress and decrease in porosity (Karig, 1993).

Fluid overpressures lead to a mechanically weak plate boundary by decreasing the normal effective stress (Byrne & Fisher, 1990; D. Davis et al., 1983; Hubbert & Rubey, 1959; Saffer & Tobin, 2011). Through its role in reducing effective stress, overpressure is widely considered to promote slow slip events (e.g., Im et al., 2020; Kodaira et al., 2004; Scholz, 1998) and other slow earthquake phenomena (non-volcanic tremor, low- and very low-frequency earthquakes) on the shallow reaches of the megathrust (e.g., Ito & Obara, 2006; Liu & Rice, 2007).

Stress changes resulting from the tectonic lateral compression in subduction zones (Figure 1) have been extensively studied through numerical geodynamic models that explore lithospheric deformation (e.g., Butler et al., 2013; Mannu et al., 2016; Morgan, 2015; Ruh et al., 2016; Spitz et al., 2020). These studies generally do not fully couple the response of pore pressure to stress changes associated with tectonic loading and deformation. The interrelation between stress, compaction, and pore pressure has been interpreted and modeled in the context of critical taper theory (e.g., Dahlen et al., 1984; D. Davis et al., 1983) using hydromechanical studies (e.g., Bekins & Dreiss, 1992; Saffer & Bekins, 2006), and with a limited number of transient geomechanical models (e.g., Borja & Dreiss, 1989; Obradors-Prats et al., 2017; Rowe et al., 2012; Sun et al., 2020). In several of these studies, porous flow and pore pressure are computed by defining fluid-source terms on the basis of a porosity field that is prescribed a priori (e.g., Bekins & Dreiss, 1992; Bekins et al., 1995; Ellis et al., 2015); other studies only consider simple constitutive models or loading paths (e.g., Skarbek & Saffer, 2009), or focus on specific areas (e.g., the toe of the wedge or the décollement; Rowe et al., 2012; Shi et al., 1989; Stauffer & Bekins, 2001).

Incorporating the full stress tensor is particularly important because accreting sediments undergo a transition from vertical uniaxial loading to lateral compression, a process that changes the horizontal stress independently from the vertical, rotates the principal stresses, and generates significant deviatoric stresses (Figure 1, e.g., Karig, 1986). The importance of considering the lateral tectonic stress in pressure estimates has long been recognized (e.g., Kitajima & Saffer, 2012; Neuzil, 1995; Tsuji et al., 2008). More recently, the role of mean stress has been incorporated in numerical models (Ellis et al., 2019; Sun et al., 2020) and site-specific investigations (Flemings & Saffer, 2018; Zhang et al., 2021). However, only a few poromechanical studies have quantitatively considered the effects of deviatoric stress on compaction and pressure generation as subduction systems develop and evolve (Obradors-Prats et al., 2017; Rowe et al., 2012).

In this work, we employ the critical state soil mechanics framework (Roscoe et al., 1958; Wood, 1990) to couple stress, strain, porosity, and pore pressure in the non-uniaxial strain environment of accretionary wedges. We first use Modified Cam Clay (MCC) and analytically quantify the contribution of mean and shear stress to compaction and pressure generation to develop insights into the processes that drive overpressure. We demonstrate that shear-induced pressures increase more rapidly than mean-stress-induced pressures near the trench, whereas pore-pressure change is proportional to mean stress change deeper inside the wedge. We then develop large-strain, evolutionary, transient numerical geomechanical models to study the coupling between tectonic loading, fluid flow, compaction, permeability, and strength in both hanging wall and the footwall. In these numerical models we employ SR3, a critical state formulation more complex than MCC. We find a rapid increase in overpressure across the trench, which is sufficiently large to outpace the increase in overburden stress. This results in higher overpressures in the hanging wall compared to the footwall. We show that both mean and shear stress contribute to pressure generation, and that the often-ignored shear-induced pressures are significant, especially in the trench area. Furthermore, we find that high overpressure reduces the normal stress at the décollement and results in a weakened megathrust that initiates a few km in advance of the trench and persists to several tens of km into the subduction zone.

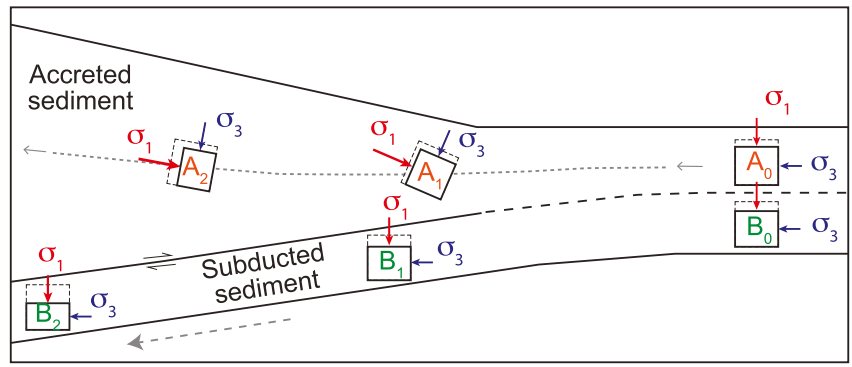

Figure 1. Schematic of an accretionary wedge with subduction paths of hanging wall (A_0–A_2) and footwall sediments (B_0–B_2). In hanging wall, transition from vertical burial (uniaxial strain) to lateral compression rotates the principal stresses; in footwall, the stress state remains approximately uniaxial.

2. Quantification of Compaction and Fluid Overpressure

2.1. Mudrock Compaction

Porous, un-cemented mudrocks compress in response to variations in both mean effective stress, σ'_m (Equation 1; see Appendix A for nomenclature) and deviatoric stress, q (Equation 2) (Wood, 1990):

$$\sigma'_m = \frac{\sigma'_1 + \sigma'_2 + \sigma'_3}{3} = \frac{\sigma'_v + \sigma'_h + \sigma'_H}{3}, \tag{1}$$

$$q = \sqrt{\frac{(\sigma_1 - \sigma_2)^2 + (\sigma_2 - \sigma_3)^2 + (\sigma_3 - \sigma_1)^2}{2}}, \tag{2}$$

where σ'_1, σ'_2, and σ'_3 are maximum, intermediate, and minimum principal effective stresses, respectively; σ_1, σ_2, and σ_3 are the corresponding total stresses; and σ'_v, σ'_h, and σ'_H the vertical, minimum horizontal, and maximum horizontal (but not necessarily principal) effective stresses. Total stresses are related to effective stresses through the effective stress principle (e.g., Terzaghi, 1925); for example, in the case of mean effective stress,

$$\sigma_m = \sigma'_m + u, \tag{3}$$

where σ_m is the mean total stress and u the pore fluid pressure.

The dependence of compaction on both mean effective and deviatoric stress is described by a family of porous elastoplastic constitutive models that are based on critical state soil mechanics (Wood, 1990). A substantial body of field and experimental data have demonstrated that this framework captures the deformation behavior of marine sediments, including those in subduction zone settings (Flemings & Saffer, 2018; Hauser et al., 2014; Karig, 1990; Kitajima & Saffer, 2012; Song et al., 2011). Here, we employ a simple but widely used critical state model, the MCC formulation (Roscoe & Burland, 1968; Wood, 1990) to illustrate the contribution of both mean effective stress and deviatoric stress to compaction and pressure generation.

We consider a deviatoric stress (q) versus mean effective stress (σ'_m) vs. porosity (n) space (Figure 2). We compare the porosity change caused by: (a) an increment in mean effective stress (σ'_m) with no deviatoric stress (q) change (blue path 1–2; Figure 2) and (b) the same increment in mean effective stress accompanied by the maximum possible deviatoric stress increase that brings the sediment to shear failure (red path 1–3; Figure 2). Even though both loading paths have the same change in mean effective stress (σ'_{m1} to σ'_{m2}; Figure 2), the porosity (n) decreases more along the path to shear failure (red path; Figure 2) than along the isotropic axis (blue path). This additional porosity change ($\Delta n_q = n_2 - n_3$) represents the shear-induced compaction. A simple explanation for this additional porosity loss in clay-rich sediments is that shear stress promotes more efficient packing and alignment of clay platelets (Karig, 1986).

Uniaxial strain is a common compaction path in sedimentary basins, in which the vertical stress is progressively increased due to sedimentation and burial: zero lateral strain is maintained due to symmetry in the horizontal

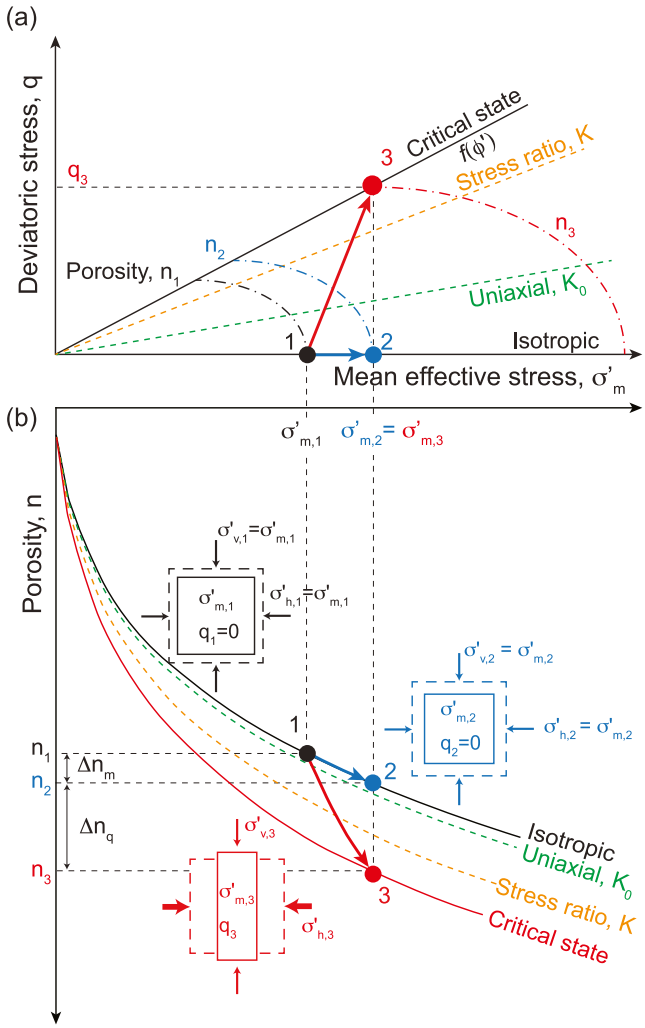

Figure 2. Schematic of the relationship between mean effective stress (σ'_m), deviatoric stress (q), and porosity (n) as described by the critical state theory (Wood, 1990). (a) Mean effective stress (σ'_m; Equation 1) versus deviatoric stress (q; Equation 2). Along the isotropic line there is no deviatoric stress. The critical state line describes the maximum deviatoric stress the sediment can support at a given mean effective stress. Compaction along paths with constant q/σ'_m ratio is represented by lines with constant slope (Equation 6, dashed orange line; Equation 5: uniaxial stress ratio, dashed green line). Iso-porosity lines (dotted curves) represent different combinations of mean and deviatoric stress that lead to a given porosity: with increasing deviatoric stress, lower mean effective stress is needed to compress to the same porosity. Along loading path 1–2 (blue), both vertical and horizontal stress components increase equally (deviatoric stress remains zero). Along loading path 1–3 (red), the horizontal stress increases more than the vertical, resulting in deviatoric stress, q_3. (b) Mean effective stress (σ'_m) versus porosity (n). For the same increment in mean effective stress, a trajectory along the isotropic line results in less porosity loss than along the critical state line. Even though the mean effective stress increase is the same in both loading paths ($\sigma'_{m,1}$ to $\sigma'_{m,2} = \sigma'_{m,3}$), the deviatoric stress in path 1–3 changes by q_3, driving additional porosity decrease ($\Delta n_q = n_2 - n_3$).

plane. Along this loading path (dashed green, Figure 2) the ratio of horizontal to vertical effective stress remains approximately constant, and is known as the uniaxial stress ratio, K_0:

$$K_0 = \frac{\sigma'_h}{\sigma'_v}. \tag{4}$$

Combining Equations 1–4, the slope of the uniaxial compaction path in the $q - \sigma'_m$ space is constant, and a function of K_0 (dashed green line, Figure 2a):

$$\eta_{K_0} = \frac{q_{K_0}}{\sigma'_{m,K_0}} = \frac{3(1-K_0)}{(1+2K_0)}. \tag{5}$$

Non-uniaxial strain conditions that maintain a constant ratio of minimum to maximum principal effective stress, K, also follow a linear path in $q - \sigma'_m$ space with slope given by (dashed orange line, Figure 2a):

$$\eta_K = \frac{q}{\sigma'_m} = \frac{3(1-K)}{(1+2K)}, \tag{6}$$

where $K = \frac{\sigma'_3}{\sigma'_1}$; under a triaxial stress state, $K = \frac{\sigma'_h}{\sigma'_v}$

The critical state line is a special case that describes the maximum deviatoric stress, q_f, that the sediment can withstand under a given mean effective stress. The slope of this line (M; black line in Figure 2) is a function of the friction angle of the material, ϕ'. In conventional triaxial compression ($\sigma'_1 > \sigma'_2 = \sigma'_3$), and for a cohesionless material,

$$\eta_{cs} = \frac{q_f}{\sigma'_m} = M = \frac{6\sin\phi'}{3 - \sin\phi'}. \tag{7}$$

Combining Equations 6 and 7, we obtain the generalized stress ratio that does not assume a constant ratio of minimum to maximum principal effective stress:

$$\eta = \frac{q}{\sigma'_m} = \frac{q}{q_f} M. \tag{8}$$

This shear-stress ratio, η, varies between 0 (isotropic stress state) and M (shear failure) and represents the deviatoric stress, q, relative to its value at critical state, q_f.

In triaxial compression loading mode, and for cohesionless sediments, the critical state line in the MCC formulation is equivalent to the Mohr-Coulomb failure line (Roscoe & Burland, 1968). In plane-strain loading mode, the MCC critical state line is steeper than the Mohr-Coulomb shear failure line, η_τ (Roscoe et al., 1958). η_τ is a function of all principal stresses; in the average stress ($\frac{\sigma'_1+\sigma'_3}{2}$) and maximum shear stress ($\frac{\sigma'_1-\sigma'_3}{2}$) space, it simplifies to:

$$|\eta_\tau| = \sin\phi'. \tag{9}$$

In active and growing critical accretionary wedges, where we commonly assume plane-strain deformation and sediments to be at Coulomb failure under lateral compression (e.g., Karig, 1990; K. L. Wang & Hu, 2006), the stress state is described by η_τ (Flemings & Saffer, 2018).

2.2. Mean-Stress- and Shear-Induced Compaction

We describe the evolution of strain with progressive loading. We decompose the volume strain into a component driven by mean effective stress, $d\sigma'_m$, and a component driven by deviatoric stress, dq:

$$\frac{d\varepsilon_v}{dt} = \xi_m \frac{d\sigma'_m}{dt} + \xi_q \frac{dq}{dt} = \xi_m \frac{d\sigma_m - du}{dt} + \xi_q \frac{dq}{dt}, \tag{10}$$

where ξ_m represents the mean stress loading efficiency, ξ_q is the shear stress loading efficiency, and t the time. The loading efficiencies in Equation 10 have the same units as compressibility and represent the increment in volumetric strain resulting from an increment in mean-effective and shear stress respectively. σ_m, σ'_m, and u are related through the effective stress principle (Equation 3).

Using the MCC framework, the loading efficiencies can be expressed as (Appendix B, Equations B1–B10):

$$\xi_m = \left[\left(\frac{\lambda - \kappa}{1+e}\right)\left(\frac{M^2 - \eta^2}{M^2 + \eta^2}\right) + \frac{\kappa}{1+e}\right]\left(\frac{1}{\sigma_m - u}\right), \tag{11}$$

$$\xi_q = \left(\frac{\lambda - \kappa}{1+e}\right)\left(\frac{2\eta}{M^2 + \eta^2}\right)\left(\frac{1}{\sigma_m - u}\right), \tag{12}$$

where κ is the elastic unloading modulus, λ is the elastoplastic loading modulus, and M the slope of the critical state line (all three of these are material properties), η is the shear-stress ratio (Equation 6), and e is the void ratio, which is related to porosity, n:

$$e = \frac{n}{1-n}, \tag{13}$$

Equation 10, together with Equations 11 and 12, describes the volume change for an increment of loading as a function of (a) both mean and deviatoric stress changes ($d\sigma_m$, dq); (b) material parameters (friction angle and compressibility; e.g., λ, κ, M) and (c) the initial stress state, that is, the position of the sediment in porosity—mean effective stress ($\sigma_m - u$)—shear stress space (e.g., Figure 2) before the application of the loading increment ($d\sigma_m$, dq).

2.3. Mean-Stress- and Shear-Induced Fluid Overpressure Evolution

Assuming conservation of fluid mass in a deforming porous medium, Darcy's law, and incompressible solid grains, the change in volumetric strain can be expressed as (Appendix B, Equations B11–B16):

$$\frac{D\varepsilon_v}{Dt} = \left(\beta_f\left(\frac{e}{1+e}\right)\right)\frac{Du}{Dt} - \frac{1}{\rho_f}\nabla\cdot\left(\frac{\rho_f k}{\mu}\nabla\cdot u_e\right). \tag{14}$$

Where ρ_f is the density of fluids, μ is the viscosity of water, k the intrinsic permeability, and u_e the overpressure. The overpressure is the difference between pore fluid pressure, u and hydrostatic pore pressure u_h:

$$u_e = u - u_h. \tag{15}$$

Substitution of Equation 10 into Equation 14 then yields:

$$\left(\beta_f\left(\frac{e}{1+e}\right) + \xi_m\right)\frac{Du}{Dt} = \xi_m \frac{D\sigma_m}{Dt} + \xi_q \frac{Dq}{Dt} + \frac{1}{\rho_f}\nabla\cdot\left(\frac{\rho_f k}{\mu}\nabla\cdot u_e\right). \tag{16}$$

$$\text{With } S = \beta_f \frac{e}{1+e} + \xi_m \,(\text{storage coefficient}) : \tag{17}$$

$$\frac{Du}{Dt} = \underbrace{\frac{\xi_m}{S}\frac{D\sigma_m}{Dt}}_{Du^m/Dt} + \underbrace{\frac{\xi_q}{S}\frac{Dq}{Dt}}_{Du^q/Dt} + \underbrace{\frac{1}{S\rho_f}\nabla\cdot\left(\frac{\rho_f k}{\mu}\nabla\cdot u_e\right)}_{Du_e^{\text{diss}}/Dt}. \tag{18}$$

The pore-pressure coefficients ξ_m/S and ξ_q/S are the loading efficiencies normalized by the storage coefficient and represent the increment in pore pressure resulting from an increment in mean and shear stress, respectively. They are analogous to Skempton's A and B pore-pressure coefficients (Skempton, 1954), for a generalized stress state and loading increment.

Equation 18 illustrates that three terms control overpressure generation: (a) the pressure induced by the change in mean stress (Du^m); (b) the pressure induced by the change in deviatoric (shear) stress (Du^q); and (c) the change in pressure due to flow in or out of the volume, which we term a dissipation pressure (Du_e^{diss}) because in almost all cases the sediment is compacting and thus fluid is expelled. Equation 18 is similar to that presented by Neuzil (1995) to describe the generation and maintenance of anomalous fluid pressure due to a range of geological driving mechanisms. However, unlike Neuzil's (1995) formulation, Equation 18 explicitly includes the important effect of deviatoric stress (q) on pore pressure. This effect—which is well established experimentally for normally consolidated sediments (Roscoe & Burland, 1968; Wood, 1990)—is not considered in poro-elastic models (H. Wang, 2000), or in previous models of coupled flow and deformation in subduction zones (Ellis et al., 2015; Ge & Screaton, 2005).

The fundamental form of Equation 18 is independent of the choice of constitutive model, as long as the constitutive formulation describes volumetric change as a function of both mean and deviatoric stress. Using MCC (Roscoe & Burland, 1968; Wood, 1990), we quantify the storage coefficient (similar to the loading coefficients; Equations 11 and 12):

$$S = \beta_f \frac{e}{1+e} + \xi_m = \beta_f \frac{e}{1+e} + \left[\left(\frac{\lambda-\kappa}{1+e}\right)\left(\frac{M^2-\eta^2}{M^2+\eta^2}\right) + \frac{\kappa}{1+e}\right]\left(\frac{1}{\sigma_m - u}\right). \tag{19}$$

2.3.1. Importance of Initial Stress State

The pore-pressure coefficients ξ_m/S and ξ_q/S (Equation 18) depend on the initial (pre-loading) stress state of the sediment: the mean effective stress, $\sigma'_m = \sigma_m - u$, the void ratio, e (or porosity), and the shear-stress ratio, η (Equations 11, 12, and 19). We quantify and compare these pore-pressure coefficients for initial stress states that have the same porosity (lie on the same iso-porosity curve, $n = 0.24$; inset in Figure 3a) but varying initial shear-stress ratio, η (e.g., isotropic [blue], uniaxial [orange], critical state [green], and values in-between; Figure 3a).

We find that ξ_m/S is relatively insensitive to the initial state in the $\sigma'_m - q$ space: it equals 1 if the stress state is isotropic before the application of the increment ($\eta = 0$; blue point on black line, Figure 3a), and decreases to 0.8 if the sediment is already at critical state before the application of the increment (green point on black line, Figure 3a). As a result, increments in mean-stress-induced overpressure vary between 100% and 80% of the mean-stress change, respectively.

In contrast, ξ_q/S is strongly dependent on the initial stress state. Its value is minimal at or near an initial isostatic stress state (blue point on red line, Figure 3a), and increases rapidly as the initial stress state approaches critical state (red line, Figure 3a). For typical material properties in the MCC model, ξ_q/S can increase by a factor of 20 between uniaxial and critical initial states (orange and green points on red line, Figure 3a). This quantification of ξ_q/S illustrates that shear-induced overpressure is very sensitive to the sediment shear-stress ratio and can be several times the deviatoric-stress change when the sediment is close to critical state.

The pore-pressure coefficients incrementally evolve along a loading path as a function of the evolving porosity, mean stress, and shear-stress ratio. The strong dependence of ξ_q/S on the initial state results in progressively higher shear-induced overpressures along loading paths that increase the shear-stress ratio (Figure 3b). Consider, for example, three undrained loading paths that have the same overall change in mean total stress, $d\sigma_m$ but different amounts of deviatoric stress change, dq ($\frac{dq}{d\sigma_m} = 1, 2\ 3$; blue, red, and green paths, Figure 3b). Higher $\frac{dq}{d\sigma_m}$ ratio values lead to progressively higher η values along the loading path, which accelerates the generation of shear-induced overpressures (Figure 3b). Shear-induced pressures may eventually become more significant than mean-stress-induced pressures (e.g., green vs. dashed black line, Figure 3b).

The exact value of the shear pore-pressure coefficient, ξ_q/S, depends on the choice of constitutive model and input parameters; however, the rapid increase in ξ_q/S with increasing shear-stress ratio is characteristic of critical-state

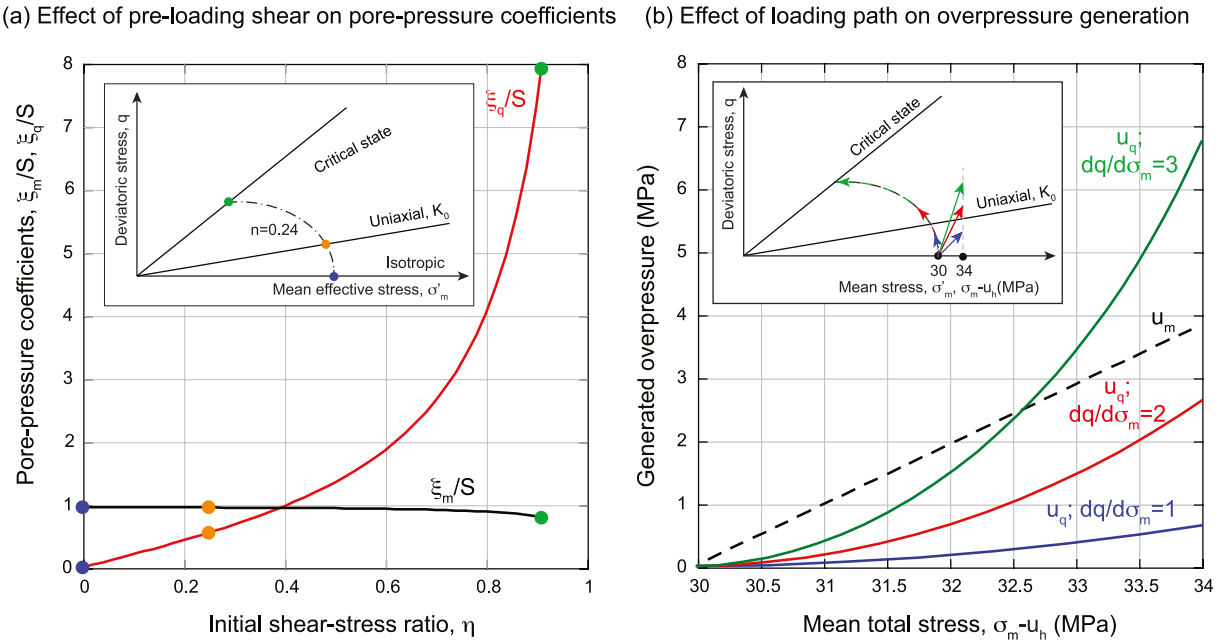

Figure 3. Importance of initial stress state for overpressure generation. (a) Pore-pressure coefficients ξ_m/S (black line) and ξ_q/S (red line) calculated as a function of the initial shear-stress ratio, η. Three stress states are highlighted: isotropic stress state ($\eta = 0$, blue), stress state at uniaxial strain ($\eta = 0.23$, orange), and stress state at critical state ($\eta = M = 0.91$, green). Initial porosity $n = 0.24$ ($e = 0.31$). Modified Cam Clay (MCC) parameters: $\kappa = 0.01$, $\lambda = 0.1$, $M = 0.91$, $e_0 = 0.65$ for $\sigma_{iso} = 1$ MPa. $\beta_f = 5 \times 10^{-4}$ MPa^{-1}. Yield and iso-porosity surfaces are assumed the same ($\kappa << \lambda$). (b) Mean-stress- (dashed black line) and shear-induced overpressures (solid lines) incrementally calculated for three undrained loading paths. All paths start at the same isotropic stress state $\sigma_{m0} - u_h = 30$ MPa and end at states with the same mean reduced total stress, $\sigma_m - u_h = 34$ MPa, and increasing deviatoric stress ($\frac{dq}{d\sigma_m} = 1$ [blue], 2 [red] and 3 [green]). Total stress paths in solid arrows, effective stress paths along iso-porosity curve. $n_0 = 0.24$; same MCC parameters as in (a).

models and highlights the importance of shear-induced pore pressures in tectonic environments undergoing a dramatic change in stress state, such as those at the trench of subduction zones, near-salt, or in extensional regimes.

2.3.2. Overpressure Generation Along Paths With Constant Shear-Stress Ratio

Along loading paths with constant shear-stress ratio, $\eta = \eta_K$ (Figure 2; $\sigma'_m - q$ space), Equation 18 simplifies to (Appendix B):

$$\frac{Du}{Dt} = \frac{\xi_K}{S_K}\frac{D\sigma_m}{Dt} + \frac{1}{S_K \rho_f}\nabla \cdot \left(\frac{\rho_f k}{\mu}\nabla \cdot u_e\right), \tag{20}$$

with a combined loading efficiency coefficient:

$$\xi_K = \left(\frac{\lambda}{1+e}\right)\left(\frac{1}{\sigma_m - u}\right), \tag{21}$$

and storage coefficient:

$$S_K = \beta_f \frac{e}{1+e} + \xi_K. \tag{22}$$

In this case, the pore-pressure coefficient, ξ_K/S_K, depends only on compressibility (λ), fluid compressibility (β_f), mean effective stress ($\sigma_m - u$) and void ratio (e). Shear-induced overpressures are still generated (and encapsulated in the term ξ_K/S_K); however, they are proportional to mean-stress-induced overpressures, and are independent of the shear-stress ratio, η (Appendix B).

Therefore, along any loading path following a constant shear-stress ratio, the generated overpressures are proportional to the change in mean total stress (Equation 20). This highlights that formulations based on the mean stress will perform well when the shear-stress ratio is not changing, regardless of the particular stress state. However, in

scenarios where the shear-stress ratio changes during loading, shear-induced pore pressures are potentially much larger and independent from changes in mean stress; in such cases, the full Equation 18 should be employed.

In the interior of active accretionary wedges, assumed to lie at a state of Coulomb failure, the shear stress ratio is constant (e.g., Dahlen et al., 1984) and pressure changes are proportional to the change in mean total stress. Furthermore, for typical compressibilities and effective stress levels, the variation of ξ_K/S_K is small and its value is greater than 0.9 but less than 1.0 (Appendix B, Figure B1). Consequently, generated overpressures are approximately equal to changes in mean stress. This reflects a value for Skempton's B coefficient approaching 1.0, which is also proposed by Neuzil (1995).

Assuming that vertical stress remains one of the three principal stresses, and that the stress ratio remains constant ($\eta = \eta_K$), the ratio of horizontal to vertical effective stress is also constant and equal to K (Equation 6). Equations 1, 3, 6, and 20 can then be re-written as a function of the vertical stress, σ_v:

$$\frac{Du}{Dt} = \frac{\xi_v}{S_v}\frac{D\sigma_v}{dt} + \frac{1}{S_v\rho_f}\nabla\cdot\left(\frac{\rho_f k}{\mu}\nabla\cdot u_e\right), \tag{23}$$

where $S_v = \beta_f \frac{e}{1+e} + \xi_v$; $\xi_v = \xi_K \frac{1+2K}{3}$ for a triaxial stress state, and $\xi_v = \xi_K \frac{2+(1+\Lambda)K-\Lambda}{3}$ for plane strain ($\Lambda = f(\eta_K, M)$; Appendix B). In such cases, the induced overpressures are proportional to the overburden change and will parallel the topographic slope. Non-vertical loading (e.g., lateral tectonic loading in accretionary wedges) is incorporated through the stress ratio, K.

2.4. Application in an Accretionary Wedge

To illustrate how the factors described above interact and drive pore fluid pressure, we first develop analytical estimates of overpressure as a sediment volume is consumed into an accretionary wedge. This approach requires simplifying assumptions, but provides insight into how the stress state, material parameters, and loading path affect overpressure development.

We consider a simplified geometry of the trench area of an accretionary wedge (Figure 4), with a sediment volume V entering the wedge (V1–V2–V3; Figure 4a). We divide the cross section into three regions (Figure 4a): (a) the area seaward of the trench, where stresses are uniaxial (Equations 4 and 5); (b) the trench area, where the horizontal stress increases and becomes the maximum principal stress; and (c) the area landward of the trench within the accretionary wedge, where sediments are at compressional frictional failure. We assume the following:

1. *Stress*: The vertical stress remains a principal stress and equal to the overburden. The horizontal effective stress increases linearly from its value under uniaxial conditions to its value at compressional failure inside the wedge (Equation 9). The intermediate principal stress is determined from Equation B28 (Roscoe & Burland, 1968).
2. *Overpressure*: There is no initial overpressure (at the location of V1). Relative overpressure, described by overpressure ratio, λ^*:

$$\lambda^* = \frac{u - u_h}{\sigma_v - u_h}. \tag{24}$$

   equals 0.4 in the wedge. This value is chosen to facilitate comparison with our numerical results. λ^* increases linearly with distance along the profile in the trench area; this assumption allows for the calculation of total overpressure, u_e.
3. *Porosity*: The initial porosity (n_0) equals 0.26 at the décollement depth seaward of the trench.

We use Equation 18 to explore how the mean (u_e^m; green) and shear (u_e^q; red) components of overpressure develop as the sediment volume traverses the trench area (Figure 4). We also obtain the dissipated pressure (black; Figure 4) $u_e^{\text{diss}} = u_e - (u_e^m + u_e^q)$. The increase in horizontal stress, due to tectonic loading, increases the mean stress and the deviatoric stress. The mean-stress-induced overpressures increase steadily across the trench area (green lines, Figure 4b). In contrast, the shear-induced overpressures initially decrease and become negative at the beginning of the transition zone. This is because deviatoric stresses decrease, as the horizontal stress increases relative to the vertical stress (red lines, Figure 4b). Once the horizontal effective stress becomes higher than the

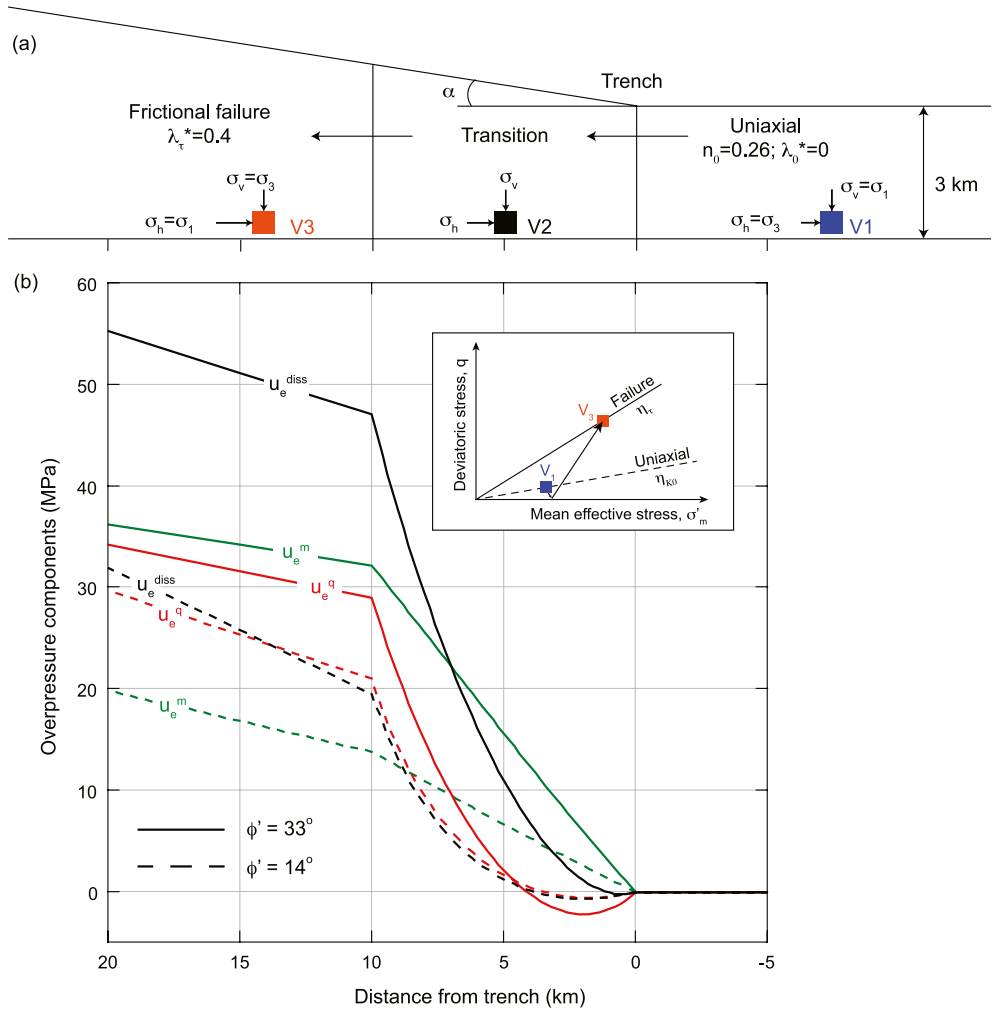

Figure 4. Analytical estimates of overpressure components as a sediment volume is consumed into an accretionary wedge. (a) Schematic of sediment path from seaward of the accretionary wedge (V1; blue), where strain conditions are uniaxial, through the transition zone (V2, black), where the horizontal stress increases, and into the wedge (V3; orange), where sediments are assumed at frictional failure. (b) Calculated mean-stress- (green lines), shear-induced overpressures (red lines), and dissipated pressures (black lines). Solid lines represent strong sediments ($\phi' = 33°$) and dashed lines weak ones ($\phi' = 14°$). Critical taper slope $a = 1.5$ and 3.1° respectively; $\beta_f = 5 \times 10^{-4}$ MPa^{-1}, $\kappa = 0.01$, $\lambda = 0.1$.

vertical, the deviatoric stress progressively increases faster than the mean effective stress. The generation of shear-induced overpressures accelerates (red lines, Figure 4b) because at each loading increment the shear-stress ratio η (Equation 8) increases, leading to a nonlinear increase in the pore-pressure coefficient ξ_q/S (Figure 3a). Inside the wedge, the shear-induced overpressures increase linearly because they are a function of mean stress changes (sediments at Coulomb failure, Equation 20).

Sediment frictional strength affects the progressive development of overpressure (solid vs. dashed lines, Figure 4). In the transition zone, stronger sediments (parameterized by the friction angle, ϕ') develop higher mean-stress-induced pressures (solid green line, $\phi' = 33°$) than weaker sediments (dashed green line, $\phi' = 14°$). Stronger sediments also develop shear-induced pressures at a higher rate (solid red line) than weaker sediments (dashed red line). This is because weaker sediments support less deviatoric stress at frictional failure (end of transition zone). In weaker sediments, shear-induced pressures at the end of the transition zone are higher than mean-stress-induced ones (dashed lines). Inside the wedge, both mean and shear overpressures increase as a function of the mean stress (Appendix B); the taper angle is set to be higher for the weaker sediments, and consequently both overpressure components (dashed lines) increase faster than in the stronger sediments (solid lines).

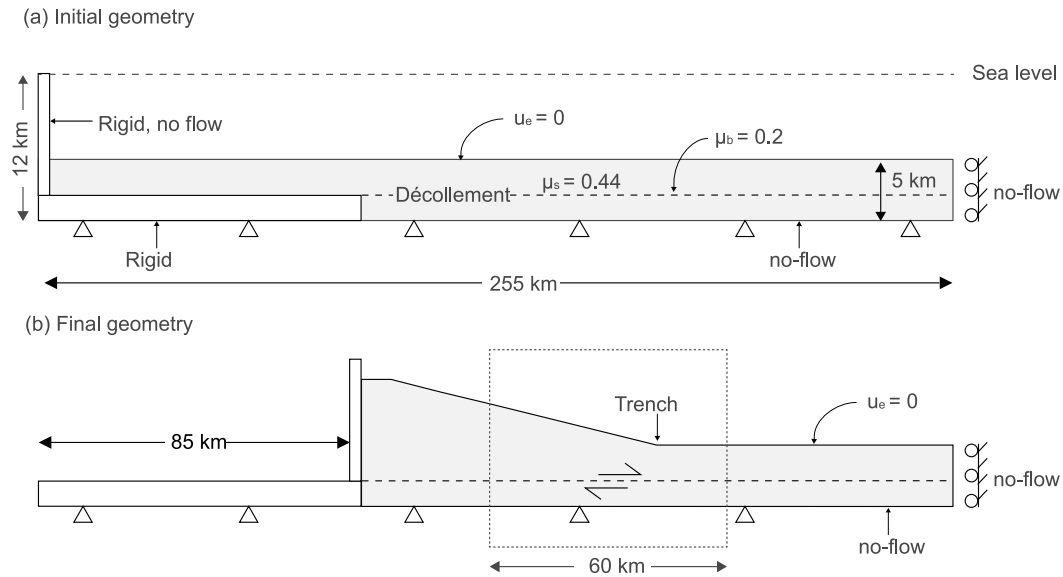

Figure 5. Model set-up and boundary conditions. (a) Initial geometry. (b) Final geometry at the end of the simulation. The vertical wall is displaced 85 km to the right. Results are plotted in the framed, 60 km-wide area near the trench. The trench is defined as the point where the surface slope angle begins to increase.

3. Numerical Geomechanical Model

We next use a transient, evolutionary numerical model to quantify the distribution and temporal evolution of stress, fluid pressure, and deformation in a growing accretionary wedge. This forward geomechanical model builds upon the concepts developed above but captures the progressive evolution of stress and strain tensors and provides the detailed spatial distribution and interrelation between stress state, pressure generation, and compaction.

3.1. Model Overview

We model a 5 km thick sedimentary section on the incoming oceanic plate (Figure 5a). A proto-décollement is located 3 km beneath the seafloor, such that the lowermost 2 km of sediments are subducted at the trench, and the uppermost 3 km are offscraped and incorporated into the growing accretionary prism. The model domain is 255 km wide. We impose a condition of zero vertical displacement along the base, and of zero horizontal displacement at the right-hand boundary (Figure 5a). To simulate the formation of an upper plate accretionary wedge, we move the left (landward) edge of the sediment above the décollement at a constant rate of 5 mm/year for a total distance of 85 km. This convergence rate is slower compared to most active margins (Clift & Vannucchi, 2004); however, for the study of pore pressure generation and dissipation, it scales with the assumed sediment thickness, which is relatively large (Clift & Vannucchi, 2004). We also conduct sensitivity analyses to further explore the role of convergence rates.

The décollement is defined as a discrete surface with a friction coefficient $\mu_b = 0.2$, a value typical for clay-rich sediments and faults (Ikari & Saffer, 2011). For simplicity, the décollement and the base of the model are set to be horizontal. The friction coefficient of the contact between the left rigid wall and the upper sediment layer (Figure 5a) is constant and equal to the sediment internal strength (set at $\mu_s = 0.44$).

The sea surface is 12 km above the base of the model and the initial pore pressure in the sediments is hydrostatic. The effective stress is zero at the top of the model (seafloor). No fluid flow is permitted across the base and side boundaries. The sea floor is a free-flow boundary. There is no flow parallel to the frictional contact that simulates the décollement; flow across the décollement contact is unrestricted, with an equivalent transverse permeability ~10 orders of magnitude higher than that of the surrounding sediments. As a result, transient flow between the hanging wall and footwall depends on sediment properties and overpressure gradient and it is unaffected by the

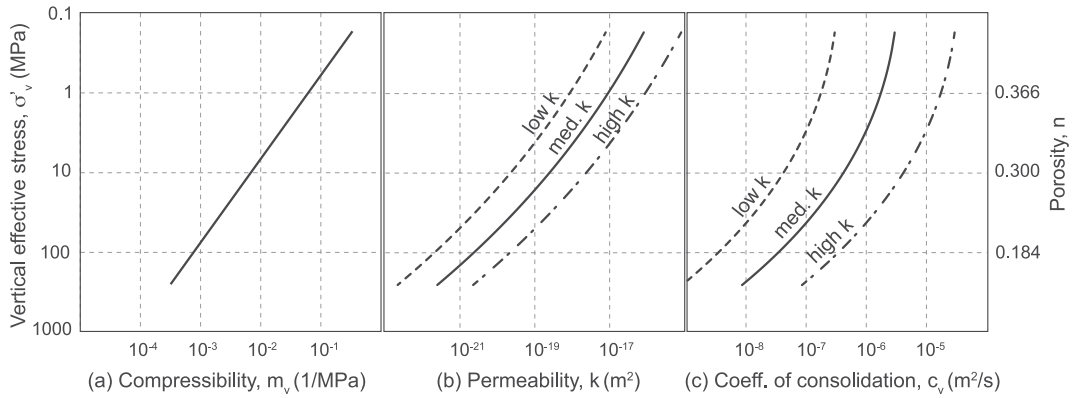

Figure 6. Variation of (a) compressibility, m_v, (b) permeability, k, and (c) the resulting coefficient of consolidation, c_v, as a function of vertical effective stress, σ'_v (left axis) and porosity, n (right axis) under uniaxial strain conditions.

frictional interface. This simulates the effect of a permeable fault zone, as has been interpreted for the décollement at many subduction zones (e.g., Saffer, 2015).

3.2. Material Properties

We treat the sediments as a homogenous, isotropic, and porous elastoplastic material described by the SR3 critical-state constitutive model (Crook, Willson, et al., 2006). SR3 captures key elements of soil and marine sediment rheology and is similar in concept to the MCC model (Crook, Owen, et al., 2006). Model input parameters are summarized in Table C1 (Appendix C) and detailed in Crook, Willson, et al. (2006).

We specify density using a porosity—effective stress relationship (Figure C1). We describe the stress-strain behavior using a formulation that relates effective mean stress (σ'_m), deviatoric stress (q), and porosity (n) (Figures C1 and C2). We define the yield surface evolution (hardening) using an empirical relationship between the compressive and tensile intercepts σ_m^c and σ_m^t of the yield surface with the isotropic axis (Figure C2) and the volumetric plastic strain, ε_v^p (Figure C3). We input the sediment friction angle that represents frictional strength in triaxial compression ($\phi'_s = 23.5°$; friction coefficient $\mu_s = 0.44$) (Bourlange et al., 2003; Ikari et al., 2009; Kopf & Brown, 2003). The frictional strength for other modes of loading (e.g., triaxial extension) is scaled as a function of the Lode angle (Crook, Willson, et al., 2006).

Transient fluid flow depends on both permeability (Figure 6b) and compressibility (Figure 6a), via the coefficient of consolidation (Terzaghi et al., 1996). Under uniaxial strain conditions:

$$c_v = \frac{k}{\mu m_v}, \text{(Figure 6c)}, \tag{25}$$

where m_v is the coefficient of volume compressibility, k the intrinsic permeability, and μ the viscosity of water.

Sediment compressibility and permeability are assumed to be isotropic and vary with porosity. In the SR3 framework, porosity is a function of mean effective stress and shear stress (Figures 2 and C1) and evolves with stress changes resulting from burial and tectonic loading. Hence, the framework describes volume and permeability changes along any given stress path. We illustrate the variation of compressibility and permeability with porosity and vertical effective stress under uniaxial strain conditions (Figures 6a and 6b). We consider three permeability-effective stress (or porosity) relationships under uniaxial strain conditions (Figure 6b), spanning the range of values reported for mudrocks entering subduction zones (Figure C4). We use the "medium permeability" relationship for the base case model and the "high" and "low" relations for sensitivity analyses.

Overall, our material calibration approach emphasizes correctly modeling the transient consolidation behavior of sediments, quantified by the coefficient of consolidation, c_v (Figure 6). The compressibility we prescribe (Figure 6a) is somewhat lower than that of shallowly buried porous mudrocks characteristic of the shallow parts of subduction zones (Flemings & Saffer, 2018; Kitajima & Saffer, 2012). However, the c_v values that result from our input compressibility and permeability values (Figure 6c) are consistent with those reported for on mudrocks

characteristic of marine environments, including Nankai (10^{-6}–10^{-8} m^2/s; Flemings et al., 2008; Schneider et al., 2009; Skarbek & Saffer, 2009).

3.3. Numerical Technique

We use the finite element program Elfen (Rockfield, 2017). Elfen has been rigorously benchmarked in a thrust-wedge study (Buiter et al., 2016) and through simulations of sandbox experiments (Crook, Willson, et al., 2006; Nollet et al., 2012). The code allows for transient hydromechanical analyses with Lagrangian and Eulerian reference frames used for the mechanical and fluid phases, respectively (Appendix C), and it supports critical state constitutive models (Perić & Crook, 2004; Thornton et al., 2011). Elfen has been used to simulate coupled geomechanical and hydrological behavior in complex, evolving geological settings, including fold and thrust belts, salt systems, extensional and compressional tectonic regimes, and carbonate platforms (Albertz & Sanz, 2012; Angus et al., 2015; Gao et al., 2018; Heidari et al., 2019; Nikolinakou et al., 2018; Nollet et al., 2012; Nolting et al., 2018; Thigpen et al., 2019; Thornton & Crook, 2014).

The program uses automated adaptive-remeshing to address excessive distortion of elements caused by large deformations. Adaptive remeshing refines the mesh in areas of high strain gradients and replaces the mesh in areas of high element distortion (Perić & Crook, 2004; Thornton et al., 2011). The finite-element mesh is composed of unstructured quadrilaterals with an initial element size of 200 m and a re-meshed size down to 50 m. The average size element size varies between 100 and 200 m.

4. Results

In simulations, the accretionary prism forms a self-similar geometry with a constant slope: the geometry, stress, and pore pressure inside this self-similar wedge do not change with time relative to the position of the advancing trench, similar to conceptual models for accretionary wedges (Bekins & Dreiss, 1992; Dahlen et al., 1984). We report horizontal distances relative to the trench (Figure 5b).

4.1. Strain Evolution

We trace the strain history of sediments above and below the décollement (Figure 7). The sediment elements are initially located outboard of the trench and are deposited under vertical uniaxial strain (burial). Hence, the maximum strain (blue, Figure 7a) is vertical. Strain in the hanging wall evolves from this uniaxial state to compressional failure inside the wedge along a zone that we term the transition zone (Figure 7). This zone extends from 10 km seaward to about 10 km landward of the trench in our base case (Figure 7). As sediments enter the transition zone, lateral tectonic loading rotates the strain ellipse, such that the maximum strain becomes sub-horizontal at the landward edge of the transition zone. During this rotation, shortening and elongation occur concurrently in the maximum and minimum strain direction, respectively. Inside the wedge, shortening continues in the sub-horizontal direction and elongation in the sub-vertical one. Overall, the minimum principal strain (ε_3) rotates away from its initial horizontal direction to a sub-vertical one. In the footwall, there is little rotation of the strain ellipse because of the limited transmission of shear across the décollement (Figure 7a). The maximum strain remains practically vertical and shortens as the thickness of the wedge increases. There is a significant contrast in sediment strains above and below the décollement (Figure 7b). This strain field is similar to observations of principal strain orientations in drill core samples from the shallow portions of well-studied accretionary wedges, including fabric orientation (Byrne & Fisher, 1990; Hamahashi et al., 2013; Morgan et al., 1994; Owens, 1993), electrical resistivity anisotropy (Henry et al., 2003), anisotropy of magnetic susceptibility (Housen et al., 1996), and P-wave velocity anisotropy (Brückmann et al., 1997).

4.2. Stress State, Overpressure, and Porosity

The stress state in the hanging wall changes from uniaxial loading seaward of the trench to lateral compressional failure inside the wedge (c.f. Figure 1). In the transition zone, increase in the lateral loading leads to an increase in the mean total stress (Figure 8a) and the deviatoric stress, q (Equation 2). The ratio q/q_f (illustrates proximity of a sediment element to shear failure; Figure 8b) increases from 0.25 seaward, where sediments are under uniaxial

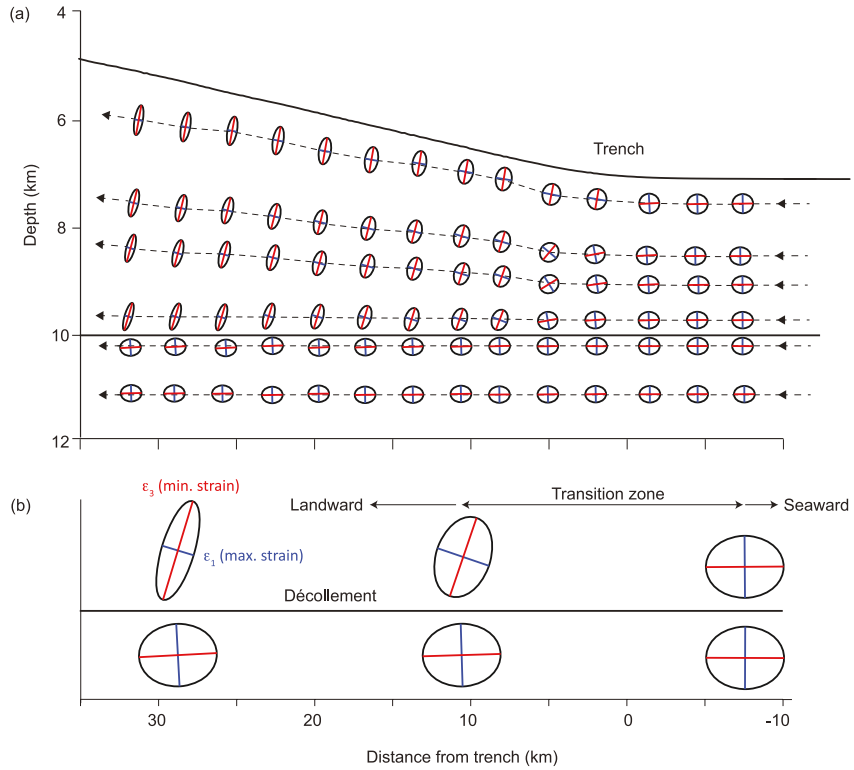

Figure 7. (a) Strain ellipse evolution of sediment elements as they enter into the accretionary wedge. Maximum principal strain (ε_1) in blue and minimum (ε_3) in red. (b) Detail of (a) showing strain ellipses of sediment elements immediately above and below the décollement at the seaward and landward ends of the transition zone, and inside the wedge.

burial stress conditions (blue color, Figure 8b) to 1 inside the wedge (red color, Figure 8b), where sediments are at Coulomb failure.

Overpressure begins to develop outboard of the trench within the transition zone (Figure 8c). In this region, there is no increase in overburden stress, because the topography is horizontal. Thus, overpressure outboard of the trench is driven exclusively by lateral loading associated with the advancing wedge. Overpressure increases rapidly across the transition zone (steep overpressure contours, Figure 8c). Landward, within the wedge ($x > 10$ km), the overpressure continues to increase in response to tectonic loading and increasing overburden. In this zone, the sediments are at frictional failure (Figure 8b), which is a stress state with constant shear-stress ratio, $\eta = \eta_\tau$, and overpressure changes are proportional to vertical effective stress changes (Equation 23). As a result, overpressure contours are parallel to the surface slope (Figure 8c). The overpressure ratio, λ^* (Equation 24), increases from 0 (hydrostatic pore pressure) to 0.5 in the wedge (Figure 8d). The nearly constant value within the wedge results from the critical state of sediments landward of the transition zone together with limited drainage. In contrast, the rapid increase of λ^* across the trench highlights the role of early tectonic loading—and concomitant changes in *stress path*—in pressure generation.

There is a discontinuity in stress across the décollement (Figures 8a and 8b). The hanging-wall sediment stress state is on or near the critical state line (A_1–A_2; circles, Figure 8f); in contrast, the footwall stress state has much lower deviatoric stresses (A_3–A_4; triangles, Figure 8f). This very different stress state above and below the décollement is independent of drainage, as it is also observed in fully drained models (gray circles and triangles, Figure 8f). Immediately below the décollement, the deviatoric stress is greater than in the uniaxial case (A_3; open white triangle, Figure 8f) and the shear-stress ratio is higher than uniaxial (Figure 8b); this is because some shear stress is transmitted to the footwall owing to the frictional strength of the décollement. With depth, shear stresses decrease toward the uniaxial value (A_3–A_4; Figure 8f). Landward, along the subduction path, the footwall shear-stress ratio increases (cyan to green contours, Figure 8b).

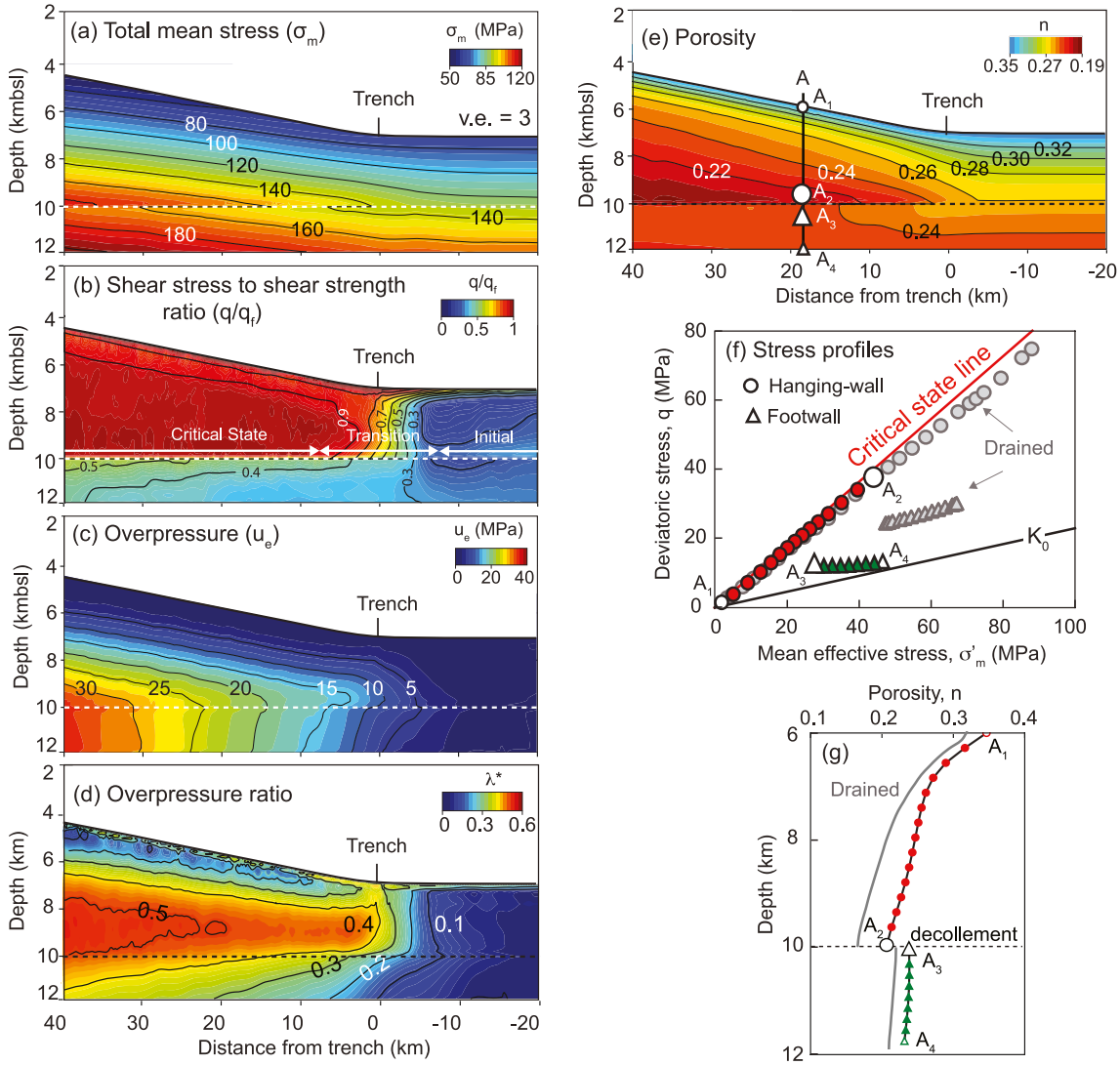

Figure 8. Color contours of: (a) mean total stress, (b) shear-stress ratio (q/q_f), (c) overpressure, (d) overpressure ratio, (e) porosity. (f) Vertical stress profile along A (A_1–A_4, shown in (e)) of mean effective stress and deviatoric stress for hanging-wall (red circles) and footwall (green triangles). A_2 and A_3 represent the stress state immediately above and below the décollement, respectively. The gray circles and triangles represent the stress state resulting from drained loading in the hanging-wall and footwall respectively (Gao et al., 2018). (g) Porosity along profile A (red: hanging-wall, green: footwall) and porosity from drained model (gray lines).

Starting seaward of the trench and for about a 30 km distance landward, the hanging wall pressures are greater than the footwall pressures (Figure 8c). In this area, tectonic loading is the main driver for overpressure and only a small percentage of the tectonic load is transmitted across the décollement (Figure 8c). Beyond 30 km landward from the trench, the pressure in the footwall exceeds that in the hanging wall. As sediments subduct, they undergo a successively increasing sediment loading by the increased height of the wedge. This overburden load eventually generates higher overpressure in the footwall than is present in the overlying wedge (Figure 8c).

There is a significant porosity offset across the décollement that begins at the trench and extends for tens of km landward (Figures 8e and 8g). Lateral tectonic loading compacts sediments above the décollement relative to those below, despite the higher overpressure (Figure 8e). Along Profile A (Figure 8e), higher mean and deviatoric stresses above than below the décollement (white circle vs. triangle, Figure 8f) lead to an offset of three porosity units (white circle vs. triangle, Figure 8g).

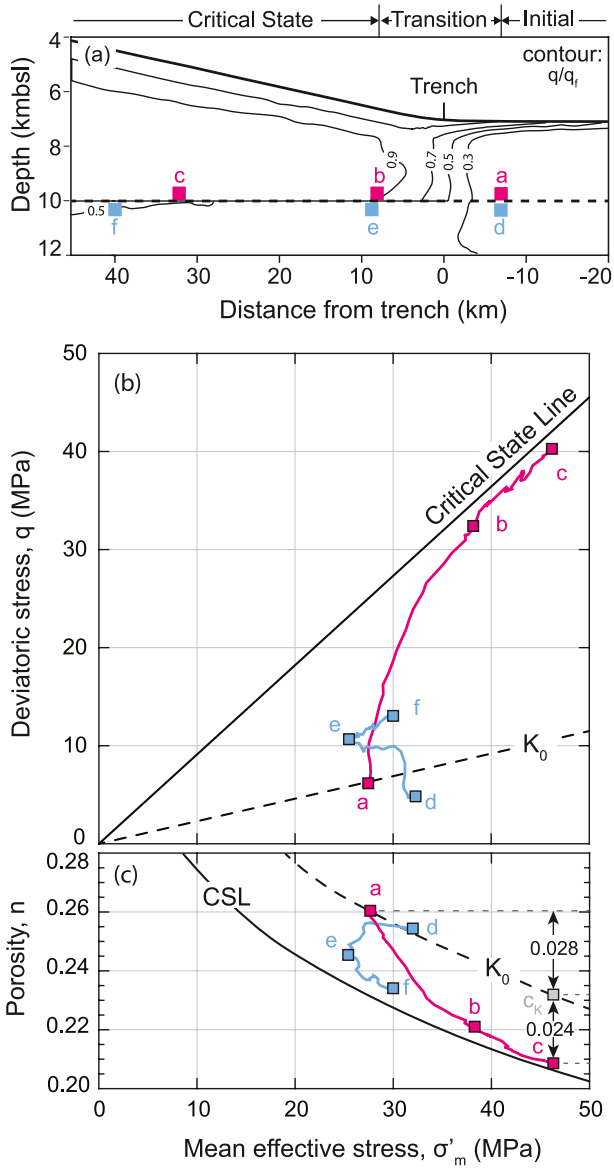

Figure 9. Stress and compaction paths for hanging-wall and footwall sediments just above and below the décollement (pink and cyan squares respectively). (a) Path of sediment volumes with contours of shear stress to shear strength ratio (q/q_f). (b) Mean effective stress—deviatoric stress space showing stress paths of hanging wall (a–c, pink) and footwall (d–f, cyan) sediments. (c) Corresponding sediment compaction paths.

4.3. Evolution of Stress State and Compaction

We track sediment elements in the hanging wall and footwall (a–c and d–f respectively; Figure 9) to illustrate the evolution of stress and porosity during progressive subduction. The elements are located just above and below the décollement. Initially, both elements are under vertical uniaxial strain conditions (a and d, Figures 9b and 9c).

As the sediment volume above the décollement passes through the transition zone (a–b, Figure 9), deviatoric stress increases rapidly (closely spaced contours in Figure 9a) because of the increase in lateral loading. Initially, the increase in mean effective stress is small (initial part of a–b is almost vertical, Figure 9b) because of the rapid increase in overpressure (Figure 8c). Eventually, lateral tectonic loading, increase in overburden, and partial drainage result in a progressive increase in mean effective stress (Figure 9b). This increase in mean effective stress together with the rapid increase in deviatoric stress leads to a porosity decrease of 0.04 units (a–b, Figure 9c). Within the wedge (b–c, Figure 9b), both mean effective and deviatoric stress continue to increase at a constant ratio η_τ (wedge sediment at Coulomb failure, Equation 9). Porosity continues to decrease but at lower rate (b–c, Figure 9c), because volume changes are proportional to changes in mean stress under constant stress ratio (Equation 20 and Appendix B).

In the footwall, shear stress transmitted across the décollement increases the deviatoric stress (Figure 9b). Below the trench (transition zone), downward flow from the more overpressured hanging wall sediments increases the footwall overpressure (Figure 8c) and decreases the mean effective stress (d–e, Figure 9b). This results in a slight porosity increase due to elastic unloading (initial part of d–e, Figure 9c). Eventually, porosity decreases because of the increase in deviatoric stress (second part of d–e, Figure 9c). As the sediment volume is further subducted beneath the wedge, both the effective stress and the shear stress increase (e–f, Figure 9b). This increase further compacts the footwall sediments (e–f, Figure 9c).

The sediment volume above the décollement is compacted 0.052 porosity units as it enters the wedge (a–c, Figure 9c). 0.028 units of this porosity loss correspond to compaction that would occur under uniaxial strain (a–c_K, Figure 9c). The remaining 0.024 units represent the additional compaction that results from the increase in shear-stress ratio from its uniaxial value to frictional failure (c_K–c, Figure 9c). This shear-related porosity loss accounts for 46% of the total porosity change and illustrates that shear-induced compaction becomes significant when the shear-stress ratio increases during the loading path (similar to shear-induced overpressures; Figure 3b).

4.4. Overpressure Mechanisms

We now explore the sources of overpressure as the sediment volume at the décollement level is incorporated into the wedge (Figure 10). Specifically, we quantify each of the terms in Equation 18 (u_e^m, u_e^q, u_e^{diss}). Initially, as the volume passes through the transition zone (a–b, Figure 10b), shear-induced overpressures (u_e^q) increase faster than mean-stress-induced pressures (u_e^m) (red vs. dashed green lines, Figure 10c). The shear-induced overpressure generation rate is double the mean-stress-induced one (Figure 10d). This is because the shear-stress ratio, η increases rapidly in the transition zone (e.g., Figures 8b and 9b). Inside the wedge, mean-stress- and shear-induced overpressures increase at comparable rates (b–c; Figures 10c and 10d). In this zone, the shear-stress ratio, η, remains constant.

Ongoing pressure dissipation (black line; Figure 10c) significantly lowers the net overpressure (blue line, Figure 10c). Dissipation is highest across the transition in stress regimes near the trench, where focused rapid

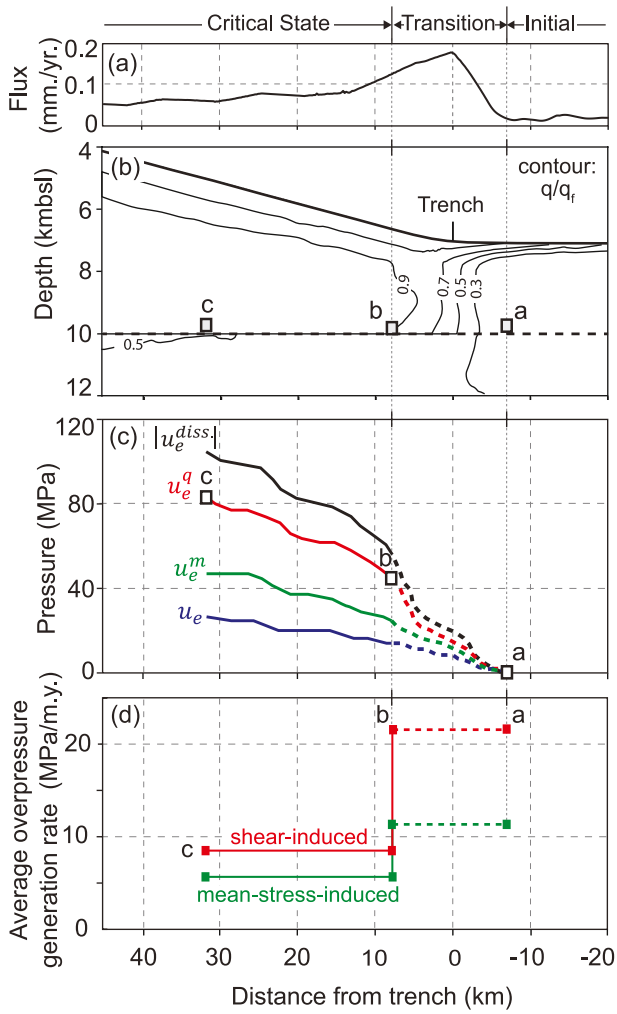

Figure 10. Overpressure components for a sediment volume just above the décollement. (a) Simulated fluid flux across the seafloor. (b) Path of sediment volume with contours of shear stress to shear strength ratio (q/q_f); Stress path in Figure 9b. (c) Components of overpressure (Equation 18 and Appendix D): mean-stress-induced pressure (u_e^m, green line) plus shear-induced pressure (u_e^q, red line) minus dissipated pressure (u_e^{diss}, black line) result in net overpressure (u_e, blue line). (d) Average shear-induced (du^q/dt; Equation 18; red line) and mean-stress induced (du^m/dt; Equation 18; green line) overpressure generation rates within the transition zone (dashed lines) and in the critical wedge (solid lines).

dewatering is generated (Figure 10a). However, the dissipation does not keep pace with the loading, and thus there is a progressive increase in overpressure as the volume passes into the subduction zone (blue line, Figure 10c).

4.5. Impact of Mudrock Permeability and Convergence Rate

We vary the mudrock permeability to study its impact on pressure and stress in the wedge (Figures 11 and 12). We consider upper and lower bounds (Figure 6b; Table 1) that envelop the range of values reported for mudrocks entering subduction zones (Appendix C, Figure C4). We also consider end-members of drained and undrained conditions (Table 1).

We evaluate overpressure profiles where the hanging wall thickness is 4 km (vertical profiles "A" marked in Figure 11). The hanging-wall overpressure ratio (λ^*) increases as permeability decreases (Figures 11a–11d). Under undrained conditions, the overpressure ratio in the wedge is very high ($\lambda^* = 0.9$, Figure 11d). λ^* equals 0.7 in the low permeability case (Figure 11c) and less than 0.25 in the high permeability case (Figure 11a). At the décollement, overpressure ranges from 26 to 12 MPa (low to high permeability, Figure 11e), and λ^* from 0.54 to 0.23 respectively (Figure 11f).

The surface slope of the wedge varies with sediment permeability. This is because permeability impacts pore pressure and thus wedge and décollement strength (e.g., D. Davis et al., 1983; Saffer & Bekins, 2006): the average wedge slope is 4.9, 4.0, 3.8, and 4.1°, for the undrained, low, medium, and high permeability case, respectively (Table 1). Higher overpressures resulting from low sediment permeability weaken the wedge more so than the décollement, leading to the counterintuitive result that the wedge is steeper in the undrained and low permeability cases than in the medium case. The surface slope increases again with further increase in permeability, because more effective drainage leads to a strengthened wedge relative to the base (e.g., D. Davis et al., 1983).

Permeability also affects the magnitude of deviatoric stresses in the accretionary wedge because sediments in the wedge are at Coulomb failure (circles, Figure 12e) and the shear-stress ratio (Equations 8 and 9) is constant. The greater wedge overpressure in models with lower permeability (Figure 11) leads to lower mean effective stress, and therefore the wedge sediments can support a smaller maximum deviatoric stress (e.g., Figure 2). As a result, deviatoric stresses in the undrained model are the lowest (gray circles) and increase as permeability is increased (blue to red to green circles, Figure 12e). The lower deviatoric stress in the wedge for poorly drained (low permeability) models results in a weaker décollement and less shear being transmitted to the footwall. Hence, footwall stresses in the undrained model are similar to a uniaxial state (gray triangles, Figure 12e), and the footwall deviatoric stresses are higher for models with higher permeability (blue to red to green triangles). The lower mean effective and deviatoric stresses associated with lower permeability result in less porosity loss in both hanging-wall and footwall sediments (Figure 12f). The porosity offset at the décollement also decreases with decreasing permeability.

We explore the influence of convergence rate on pressure and stress with three models having convergence rates of 1 mm/year (slow), 5 mm/year (medium), and 10 mm/year (high) (Table 1, Models 5, 2, and 6). The medium-convergence-rate case is the rate used in models discussed so far. Increasing the tectonic loading rate leads to higher pore pressures, as overpressure is generated significantly faster than dissipated. As a result, an increase in convergence rate has similar effects on overpressure, mean effective stress, strength, and porosity as a decrease in permeability (Appendix E).

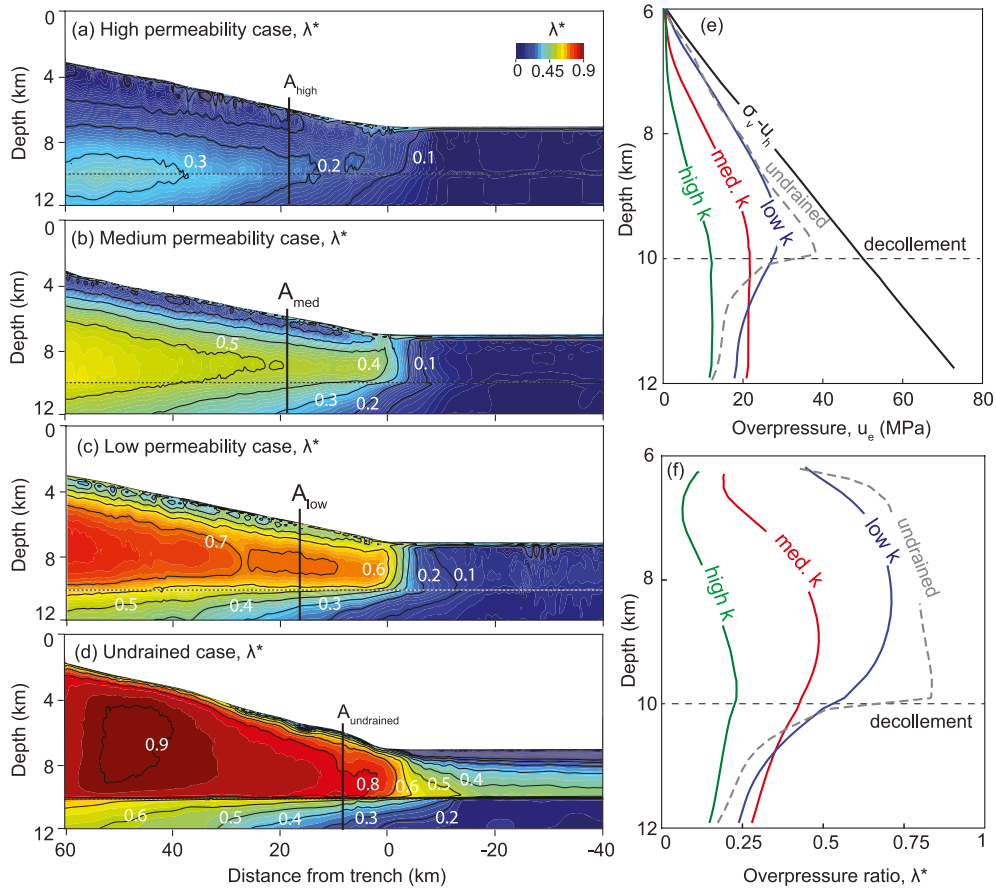

Figure 11. Impact of permeability on overpressure (Table 1, Models 1–4). (a–d) Overpressure ratio λ^* (Equation 24) for high-, medium-, low-permeability, and undrained case. (e and f) Comparison of overpressure and overpressure ratio for high (green), medium (red), low permeability (blue), and undrained models (dashed-gray), along vertical profiles A at 4 km hanging-wall thickness marked in (a–d). The undrained model calculates pressure as a function of volumetric strain only and does not simulate transient flow, leading to the observed décollement discontinuity.

5. Discussion

Figure 13 summarizes the key processes we envision as a sediment packet approaches and is incorporated into a subduction zone. Mean and shear stress in the hanging wall increase rapidly in a transition zone spanning from ~10 km seaward of the trench to ~10 km landward. This drives the rapid development of overpressure (Figure 13b), which outpaces the increase in overburden from burial. The high pore pressures reduce the vertical effective stress in the hanging wall and result in a broad zone of significantly reduced shear strength along the plate interface (Figure 13c) that initiates outboard of the trench and persists for tens of km into the subduction zone. The rapid loading across the transition zone and outermost wedge combined with partial drainage leads to focused dewatering (Figure 13a), which enables compaction of the hanging wall sediments. The distinct stress states above and below the décollement yield a porosity offset at the décollement, despite the fact that pore pressures in the hanging wall exceed those in the footwall. Landward, within the wedge, the sediments are at Coulomb failure and overpressures parallel the topographic slope. Footwall sediments are rapidly subducting beneath the hanging wall. These sediments ultimately have higher pressure than the overlying hanging wall sediments (Figure 13b). We explore these insights below.

5.1. Overpressure Generation and Its Spatial Distribution

Lateral tectonic loading increases mean and deviatoric stresses as sediment is incorporated into the accretionary wedge (Figures 8a, 8b, and 8f). This evolving stress state drives overpressures (Figures 10c and 13b) that may increase more rapidly than the overburden.

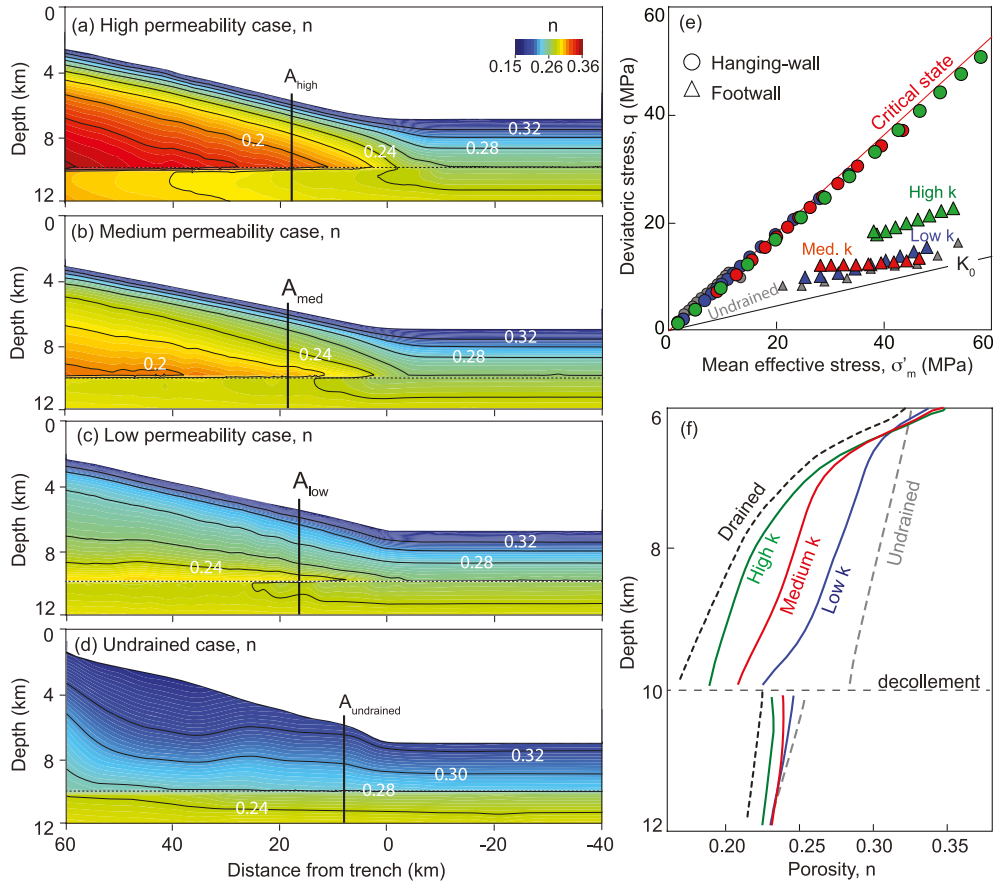

Figure 12. Impact of permeability on compaction and stress. (a–d) Porosity distribution for high-, medium-, low-permeability, and undrained case. (e) Mean effective stress and deviatoric stress along vertical profiles A marked in (a–d). Circles represent stress states in the hanging wall and triangles in footwall. (f) Porosity-depth curves for high (green), medium (red), low permeability (blue), and undrained model (dashed gray line). Drained profile from Gao et al. (2018) is shown for comparison (dashed-black line). Increase in sediment thickness in the undrained wedge leads to porosity increase.

The lateral loading extends several km seaward of the trench driving overpressures outboard of the trench (Figures 8, 10c, and 13b). The increase in pore pressure decreases the mean effective stress and hence the strength of the sediments even prior to subduction (Figure 9b). In our models, sediments seaward of the trench are not at failure. However, the increase in lateral loading together with the decrease in sediment strength could provide a mechanistic explanation for the presence of protothrust zones, which are often attributed to elevated pore pressures (e.g., Barnes et al., 2018; C. Y. Wang et al., 1994) and potentially for décollement initiation or propagation.

In the transition zone, both mean and shear stress generate overpressure and the shear-induced overpressure is twice that generated by mean stress (Figures 10c, 10d, and 13b). The rapid increase in deviatoric stress relative to mean effective stress (shear stress ratio, η; Equation 8) in this zone results in the significant shear-induced pressures, an effect not predicted in models that consider only mean-stress-induced pressure generation.

The wedge itself is at Coulomb failure (Figure 8b); in this zone the overpressure increase is proportional to the vertical stress change (overburden stress, Equation 23). Consequently, the overpressure contours parallel the topographic surface (Figure 8c) and pore pressure can be estimated from overburden as long as the significant, non-vertical stress components are incorporated (Equation 23, Section 2.3.2).

In the footwall, the stress state remains approximately uniaxial (Figure 8f)–especially for low sediment permeability and high convergence rates (Figures 12 and E2). This is because high overpressures limit the effective stresses above the décollement, minimizing the shear stresses transmitted across the décollement (e.g., Figure 8b). A near-uniaxial stress state at the footwall is consistent with observations of footwall strain (Henry et al., 2003; Housen et al., 1996) and stress states (e.g., Byrne & Fisher, 1990; Drews & Duschl, 2022) interpreted to reflect

Table 1
List of Sensitivity-Analyses Models With Summary of Key Results

Model No.	#0	#1	#2	#3	#4	#5	#6
Permeability	Drained	High	Medium	Low	Undrained	Medium	
Convergence rate (mm/year)	n/a	5				10	1
λ* at décollement	0	0.22	0.43	0.53	0.83	0.47	0.29
Porosity offset at décollement (%)	6	4	3	1	−3	2	4
Surface slope	5	4.1	3.8	4	4.9	3.7	4.1
σ_1' dip hanging wall	7.4	7.4	8	6.3	17.1	8.5	7.8
σ_x'/σ_v' hanging wall	2.4	2.4	2.5	2.7	2.3	2.5	2.4
σ_1'/σ_3' hanging wall	2.5	2.5	2.6	2.8	2.9	2.6	2.5
q/σ_m' hanging wall	0.85	0.84	0.86	0.91	0.96	0.86	0.83
σ_1' dip footwall	62	58	55	58	66.2	54.5	55.2
σ_x'/σ_v' footwall	0.76	0.83	0.9	0.91	0.87	0.89	0.87
σ_1'/σ_3' footwall	1.6	1.6	1.4	1.4	1.3	1.6	1.5
q/σ_m' footwall	0.48	0.46	0.35	0.33	0.31	0.36	0.42

Note. λ*, stress ratios and stress orientations are estimated using the average value along sediment profile A (Figures 11, 12, E1, and E2) for both hanging wall and footwall. Drained model results from Gao et al. (2018).

a uniaxial (vertical compression) path well into the subduction zone. It suggests that to first order, approaches that consider only burial below the décollement are appropriate (e.g., Skarbek & Saffer, 2009). Because of this near-uniaxial stress state, both mean and shear-induced overpressures are much lower in the footwall compared to hanging-wall (Figure 8c).

In our model, higher overpressures in the hanging wall relative to the footwall persist for several km across the transition zone and into the wedge. Farther into the interior of the wedge, pore pressure beneath the décollement exceeds that of the hanging wall. This is because footwall sediments are transported more rapidly than overlying wedge sediments (relative to a fixed position at the wedge front), which are subjected to thickening and lateral compression (Bekins & Dreiss, 1992; Bray & Karig, 1985). As a result, footwall sediments are subjected to more rapid vertical loading than hanging wall sediments at any particular location. This increased vertical loading, in combination with a greater drainage distance for fluid escape from the footwall, eventually overtakes the effect of mean-stress- and shear-induced overpressures (Figure 13b). The distance into the wedge where the hanging and footwall pressures become equal at the décollement is located at ∼25–30 km from the trench in the base model (Figure 8c) and depends on the lateral deformation rate and material properties (Figures 11 and E1).

There are also footwall overpressures ahead of the trench, where the seafloor is flat (Figure 8c); these footwall overpressures increase faster than the overburden load below the trench area (Figure 8d), leading to a local decrease in mean effective stress (Figure 9b). A source of these overpressures is downward fluid flow that occurs across the décollement because hanging-wall overpressures are greater than footwall overpressures.

5.2. Pore Pressure, Effective Stress, and Shear Strength Along the Décollement

The vertical effective stress at the décollement decreases by approximately 30% (2 MPa) over a broad region that extends from a few km in advance of the trench, across the transition zone, and persists well into the subduction zone (Figures 13b and 14b left axis). This decrease in effective stress is caused by the rapid overpressure increase in the transition zone. Shear strength (τ) along the décollement is proportional to the vertical effective stress. Thus, the decrease in effective stress at the trench corresponds to a broad and weakened region where shear strength along the plate interface is far lower than that expected for drained conditions. The width and magnitude of this weak zone increase with decreased permeability (Figure 14c) and with increased convergence rate (Appendix E).

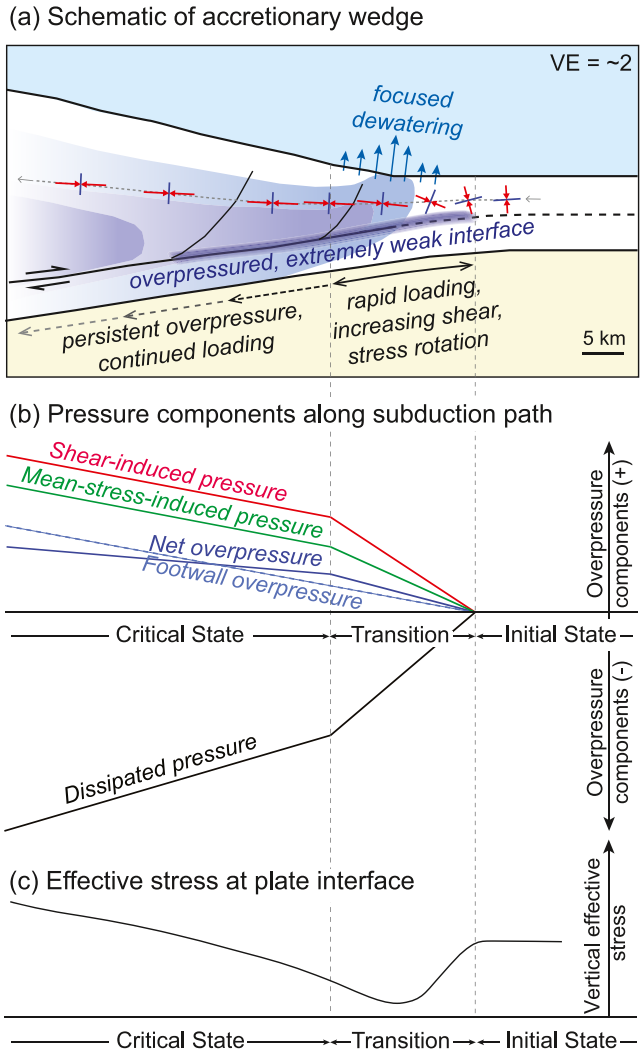

Figure 13. Schematic highlighting key insights on pore pressure and décollement strength. (a) Subduction path: red and blue arrows (maximum and minimum in-plane principal stress respectively) illustrate stress rotation from vertical burial to lateral compression along subduction path. (b) Individual contribution of overpressure components to net overpressure (blue line) along the décollement: mean-stress-induced pressures (green) plus shear-induced pressures (red) minus dissipated pressures (black) provide the net pressure (blue). Mean stress consistently drives overpressure in the accreting sediments (green); the role of shear stress is pronounced in the transition zone (red); dissipation prevails throughout the wedge and increases in the transition zone (black line in (b) and blue arrows in (a)). Footwall pressure (dashed blue line) becomes higher than hanging-wall pressure (solid blue line) landward. (c) Effective-stress decrease along the décollement in the trench area results in a weak plate interface (purple in (a)).

The reduced effective normal stress in the transition zone, together with increasing sediment stiffness due to progressive compaction, may drive stable and/or slow slip in this region (e.g., Kodaira et al., 2004; Liu & Rice, 2007; Moore & Saffer, 2001; Scholz, 1998). Slip instability is commonly described by the force balance for a simplified 1-D spring-slider model (e.g., Scholz, 2012): stable slip can occur if:

$$K > K_c. \tag{26}$$

K is the stiffness of the loading system, which is described by the sediment elastic moduli (determined in our model by the evolving porosity). K_c is the rheological stiffness of the fault, described by:

$$K_c = \sigma_n' \frac{b-a}{D_c}, \tag{27}$$

where $(b - a)$ describes the velocity dependence of friction, D_c the slip distance over which slip weakening occurs, and σ_n' is the effective normal stress.

Our results indicate that in the outer several tens of km of the subduction zone, effective stresses remain low (Figure 14). In addition, compaction (Figure 8) increases the sediment elastic moduli (and hence K) in the hanging wall. These two effects—low σ_n' and increasing K—promote stable slip in the transition zone, and potentially for several tens of km landward. This is consistent with the increasingly common observation of slow earthquakes on the shallow parts of the plate interface (e.g., slow slip events [Araki et al., 2017; Sugioka et al., 2012; Wallace et al., 2017], low-frequency earthquakes [Ito & Obara, 2006], and low-frequency tremors [Obana & Kodaira, 2009]). Although it suppresses nucleation of unstable slip locally, the extension of the weak interface for tens of km into the subduction zone may at the same time facilitate large coseismic ruptures initiating at greater depth that propagate to the trench (Kodaira et al., 2012; Kozdon & Dunham, 2013; Wallace et al., 2017; C. Y. Wang et al., 1994).

5.3. Consolidation and Dewatering

The hanging wall sediments are more compacted than the footwall sediments in the transition zone even though the hanging wall has greater overpressure (Figures 8e and 8g). The increase in mean and deviatoric stress combines with fluid expulsion to drive this porosity decrease. This provides a hydromechanical explanation for the abrupt porosity decrease observed across the décollement (e.g., Bangs et al., 1990; Costa Pisani et al., 2005; Flemings & Saffer, 2018; Park et al., 2010; Saffer & Tobin, 2011; E. Screaton et al., 2002). Tectonic loading also leads to porosity loss seaward of the trench (Figure 8e), which is consistent with observations of gradually increasing P-wave velocity and electrical resistivity across the protothrust zone offshore S. Hikurangi (Chesley, 2022).

Fluid expulsion is focused around the trench (Figure 10a). This is consistent with: (a) the prevalence of fluid expulsion features across and near the trench at several subduction zones, including seeps (e.g., Suess et al., 1998) or elevated surface heat-flow (E. E. Davis et al., 1990; Yamano et al., 1992); and (b) with porosity and seismic velocity data suggesting that compaction is most pronounced in this zone (Karig, 1990; C. Y. Wang et al., 1994; Yuan et al., 1994). It is also consistent with early (non-coupled) models of dewatering rates in accretionary prisms (Bekins & Dreiss, 1992) which have shown that the amount of fluid expelled increases when tectonic porosity loss is (empirically) included.

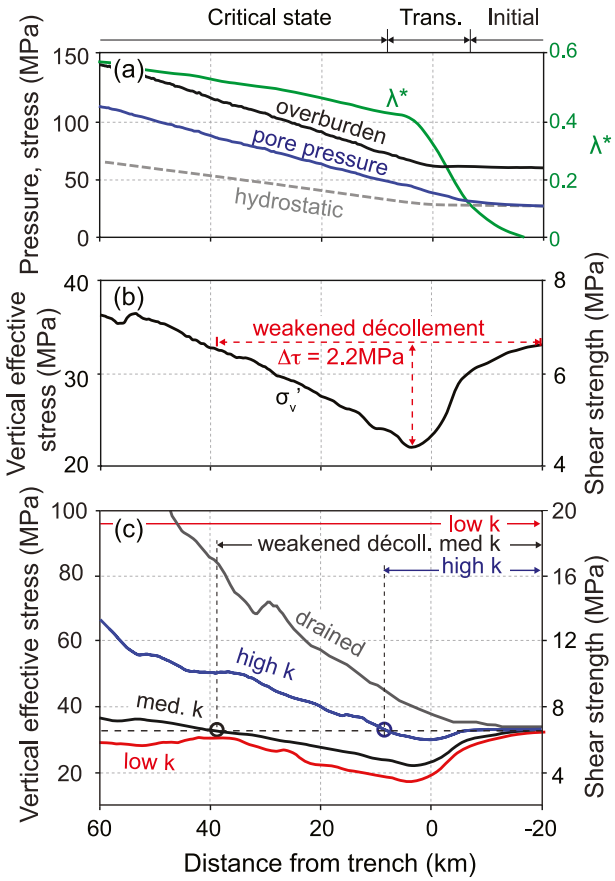

Figure 14. Pressure, effective stress, and strength at the décollement. (a) Hydrostatic pressure (gray dashed line), pore pressure (blue line), and overburden stress (black line), referenced to the seafloor. The overpressure ratio λ* (Equation 24; green line & right axis) is also shown. (b) Distribution of vertical effective stress (σ'_v) and shear strength ($\tau = \mu_b(\sigma_v - u) = \mu_b\sigma'_v$). (c) Impact of mudrock permeability on the vertical effective stress and shear strength along décollement. The dashed horizontal lines in panels (b and c) mark the effective stress and shear strength value at the uniaxial, seaward far-field. Circles in (c) mark the location landward where shear strength returns to its uniaxial value.

5.4. Broader Insights

Our evolutionary geomechanical model simulates large scale deformation of an accretionary wedge with a soil model that considers the effect of both mean and deviatoric stress. Very few studies have incorporated critical-state models to couple deformation and porous-fluid flow in accretionary wedges (Obradors-Prats et al., 2017; Rowe et al., 2012). Our work contributes the modeling of large-scale deformation and, more importantly, the quantification of mean-stress- and shear-induced overpressures in a continuing effort to understand stress, pore pressure, and deformation in the shallow parts of subduction zones.

We show that the pore pressure response is proportional to changes in mean stress in tectonic environments characterized by a constant shear-stress ratio (e.g., Coulomb failure or uniaxial). This illuminates why models that describe deformation and fluid flow in subduction zones as a function of only mean stress are successful within accretionary wedges (e.g., Henry & Wang, 1991; Neuzil, 1995; Stauffer & Bekins, 2001).

We also show that shear-induced overpressures are not proportional to changes in mean stress in systems where the shear-stress ratio changes. An example such system is the transition zone in an accretionary wedge. In these environments, shear-induced pressures can be several times higher than the mean-stress-induced pressures. Hence, it is important to capture the full pore-pressure response including the deviatoric term in Equation 18.

Our quantification of mean-stress- and shear-induced overpressures could help improve pore-pressure estimates from field data. Such workflows are based on experimental measurements on recovered cores (e.g., French & Morgan, 2020; Karig, 1993; E. Screaton et al., 2002; Zhang et al., 2021), seismic velocity measurements (e.g., Calahorrano et al., 2008; Park et al., 2010; Tobin & Saffer, 2009; Tsuji et al., 2008), or acoustic log data (e.g., Kitajima et al., 2017) and often introduce simplified assumptions (e.g., uniaxial strain).

5.5. Model Limitations and Enhancements

Our model does not incorporate strain softening and the decrease in frictional strength typically associated with progressive displacement along shear zones (i.e., from the development of shear fabric). Nor do we model the formation or propagation of discrete faults. Yet, accretionary wedges are pervasively faulted, and we expect that strain localization on individual faults will locally alter the distribution of both stress and permeability and may impact the surface topography and the process of accretion. Such faults would also potentially change patterns of porous fluid flow and sediment overpressure by facilitating drainage, although in fine-grained mudrocks the low matrix permeability would still serve as the primary control on drainage state (Saffer, 2015). We model the décollement as a discrete contact surface, and do not simulate fluid flow along the décollement. The presence of a permeable décollement would allow for significant pressure dissipation as has been proposed by others (Party, 1987; E. Screaton et al., 2000). We also assume a high vertical permeability across the décollement and do not consider local or temporal variations of this permeability. Such changes in the décollement flow properties will alter the overpressure distribution in both hanging wall and footwall in the near-field of the fault.

Future model enhancements could consider spatial heterogeneity of material properties (e.g., different lithologies, layering), cementation, thermal processes (e.g., thermally enhanced compaction), or dehydration reactions.

6. Summary

It is commonly understood that seaward of the accretionary wedge, sediments are deposited under uniaxial strain whereas inside the wedge sediments are at Coulomb failure. We simulate both analytically and with a large-strain numerical model the evolution in stress, pore pressure, and porosity as the stress state transitions from uniaxial to Coulomb failure.

Lateral tectonic loading increases the mean and deviatoric stress ahead of and across the trench area. Both stress changes contribute to a rapid increase in overpressure in this transition zone. In turn, high overpressures result in a weakened décollement that onsets ahead of the trench and persists tens of km into the subduction zone. Our results provide mechanisms for explaining stable sliding at the trench and the presence of protothrust zones.

Our approach incorporates the effect of both deviatoric and mean-stress changes on compaction and overpressure generation. We show that shear-induced compaction should be explicitly included in tectonic environments that undergo a dramatic change in stress state, such as at the trench of subduction zones or near salt bodies in sedimentary basins. The shear-induced compaction changes the sediment properties and drives significant overpressures. In contrast, we find that in areas where the ratio between deviatoric and mean-effective stress is not changing, such as within accretionary wedges, established approaches that depend on the mean stress perform adequately.

Appendix A: Nomenclature

Symbol	Description	Dimensions
c_v	Coefficient of consolidation	$M^0L^2T^{-1}$
e	Void ratio	-
g	Gravity acceleration	M^0LT^{-2}
k	Intrinsic permeability	L^2
L	Continuum mechanics differential operator	$M^0L^{-1}T^0$
m_v	Mudrock compressibility	$M^{-1}LT^2$
n	Porosity	-
q	Deviatoric stress	$ML^{-1}T^{-2}$
q_f	Shear strength	$ML^{-1}T^{-2}$
q_{fl}	Volume flux of fluid relative to solid matrix	M^0LT^{-1}
S	Storage coefficient	$M^{-1}LT^2$
t	Time	T^1
u	Pore pressure	$ML^{-1}T^{-2}$
u_e	Overpressure	$ML^{-1}T^{-2}$
u_h	Hydrostatic pressure	$ML^{-1}T^{-2}$
u^m	Mean-stress-induced pressure	$ML^{-1}T^{-2}$
u_e^m	Mean-stress-induced overpressure	$ML^{-1}T^{-2}$
u^q	Shear-induced pressure	$ML^{-1}T^{-2}$
u_e^q	Shear-induced overpressure	$ML^{-1}T^{-2}$
u_e^{diss}	Dissipated overpressure	$ML^{-1}T^{-2}$
v	Fluid volume flux per unit area	M^0LT^{-1}
α	Critical taper angle	
$\beta_{s'}$	Solid-grain compressibility relating to stress	$M^{-1}LT^2$
β_s	Solid-grain compressibility relating to pressure	$M^{-1}LT^2$
β_f	Fluid compressibility	$M^{-1}LT^2$
$\Delta\varepsilon$	Incremental total-strain tensor	-

Symbol	Description	Dimensions
$\Delta\varepsilon_e$	Incremental elastic-strain tensor	-
$\Delta\varepsilon_p$	Incremental plastic-strain tensor	-
ε_v	Volumetric strain	-
η	Shear stress ratio	-
λ^*	Overpressure ratio	$ML^{-1}T^{-2}$
u	Fluid viscosity	$ML^{-1}T^{-1}$
μ_b	Basal friction coefficient	-
μ_s	Sediment internal friction coefficient	-
ξ_m	Mean stress loading efficiency	$M^{-1}LT^2$
ξ_a	Shear stress loading efficiency	$M^{-1}LT^2$
ρ_b	Saturated bulk density	$ML^{-3}T^0$
ρ_f	Fluid density	$ML^{-3}T^0$
ρ_s	Grain density	$ML^{-3}T^0$
$\boldsymbol{\sigma}$	Total stress tensor	$ML^{-1}T^{-2}$
σ_1	Maximum principal stress	$ML^{-1}T^{-2}$
σ_2	Intermediate principal stress	$ML^{-1}T^{-2}$
σ_3	Minimum principal stress	$ML^{-1}T^{-2}$
$\boldsymbol{\sigma}'$	Effective stress tensor	$ML^{-1}T^{-2}$
σ'_1	Maximum principal effective stress	$ML^{-1}T^{-2}$
σ'_2	Intermediate principal effective stress	$ML^{-1}T^{-2}$
σ'_3	Minimum principal effective stress	$ML^{-1}T^{-2}$
σ_h	Horizontal total stress	$ML^{-1}T^{-2}$
σ'_h	Horizontal effective stress	$ML^{-1}T^{-2}$
σ_m	Mean total stress	$ML^{-1}T^{-2}$
σ'_m	Mean effective stress	$ML^{-1}T^{-2}$
σ_v	Vertical total stress	$ML^{-1}T^{-2}$
σ'_v	Vertical effective stress	$ML^{-1}T^{-2}$
σ^c_m	Compressive intercept (SR3)	$ML^{-1}T^{-2}$
σ^t_m	Tensile intercept (SR3)	$ML^{-1}T^{-2}$
τ	Shear strength	$ML^{-1}T^{-2}$
ϕ'_s	Sediment internal friction angle	-

Appendix B: Mean and Shear Components of Overpressure, and Formulation of Pore-Pressure Coefficients Using Modified Cam Clay.

In the MCC model, a volumetric strain increment, $d\varepsilon_v$, consists of an elastic ($d\varepsilon^e_v$) and a plastic component ($d\varepsilon^p_v$):

$$d\varepsilon_v = d\varepsilon^e_v + d\varepsilon^p_v \tag{B1}$$

The volumetric components are calculated as a function of the current state (stress and void ratio) and the loading increment. The elastic volumetric strain increment is:

$$d\varepsilon^e_v = \frac{\kappa}{1+e}\frac{d\sigma'_m}{\sigma'_m}, \tag{B2}$$

where κ is the elastic unloading modulus, $d\sigma'_m$ is the mean effective stress increment, and e the void ratio; the elastoplastic volumetric strain increment is:

$$d\varepsilon_v^p = \frac{\lambda-\kappa}{1+e}\left(\left(\frac{2\sigma'_m}{\sigma'_e}-1\right)\frac{d\sigma'_m}{\sigma'_m}\right)+\left(\frac{\lambda-\kappa}{1+e}\right)\left(\frac{2q}{M^2\sigma'_m\sigma'_e}\right)dq, \tag{B3}$$

where λ is the elastoplastic loading modulus, dq the deviatoric stress increment, M the slope of the critical state line, which is a function of the sediment internal friction angle:

$$M = \frac{6\sin\Phi'_s}{3-\sin\Phi'_s}, \tag{B4}$$

and σ'_e the equivalent effective stress, obtained from the description of iso-porosity curves:

$$\frac{\sigma'_m}{\sigma'_e} = \left(\frac{M^2}{M^2+\eta^2}\right)^{1-\kappa/\lambda} \tag{B5}$$

$$\text{where } \eta = \frac{q}{\sigma'_m} \text{ is the shear} - \text{stress ratio.} \tag{B6}$$

Assuming that $\kappa \ll \lambda$, the total volumetric strain rate is:

$$\frac{d\varepsilon_v}{dt} = \left(\left(\frac{\lambda-\kappa}{1+e}\right)\left(\frac{M^2-\eta^2}{M^2+\eta^2}\right)+\frac{\kappa}{1+e}\right)\left(\frac{1}{\sigma'_m}\right)\frac{d\sigma'_m}{dt}+\left(\frac{\lambda-\kappa}{1+e}\right)\left(\frac{2\eta}{\sigma'_m(M^2+\eta^2)}\right)\frac{dq}{dt}. \tag{B7}$$

and, using the effective stress principle ($\sigma_m = \sigma'_m + u$):

$$\begin{aligned}\frac{d\varepsilon_v}{dt} = &\left[\left(\frac{\lambda-\kappa}{1+e}\right)\left(\frac{M^2-\eta^2}{M^2+\eta^2}\right)+\frac{\kappa}{1+e}\right]\left(\frac{1}{\sigma_m-u}\right)\cdot\frac{d\sigma_m}{dt}\\ &-\left[\left(\frac{\lambda-\kappa}{1+e}\right)\left(\frac{M^2-\eta^2}{M^2+\eta^2}\right)+\frac{\kappa}{1+e}\right]\left(\frac{1}{\sigma_m-u}\right)\cdot\frac{du}{dt}\\ &+\left(\frac{\lambda-\kappa}{1+e}\right)\left(\frac{2\eta}{(\sigma_m-u)(M^2+\eta^2)}\right)\cdot\frac{dq}{dt}.\end{aligned} \tag{B8}$$

Equation B8 provides the loading efficiencies: mean-stress loading efficiency, ξ_m (Equation 11):

$$\xi_m = \left[\left(\frac{\lambda-\kappa}{1+e}\right)\left(\frac{M^2-\eta^2}{M^2+\eta^2}\right)+\frac{\kappa}{1+e}\right]\left(\frac{1}{\sigma_m-u}\right), \tag{B9}$$

and shear-stress loading efficiency, ξ_q (Equation 12):

$$\xi_q = \left(\frac{\lambda-\kappa}{1+e}\right)\left(\frac{2\eta}{M^2+\eta^2}\right)\left(\frac{1}{\sigma_m-u}\right) \tag{B10}$$

The conservation of fluid mass in a deforming porous medium is (Palciauskas & Domenico, 1989):

$$\frac{1}{V}\frac{DV}{Dt}+\left(\frac{1-n}{\rho_s}\right)\frac{D\rho_s}{Dt}+\left(\frac{n}{\rho_f}\right)\frac{D\rho_f}{Dt}+\frac{1}{\rho_f}\nabla\cdot(\rho_f q_{\mathrm{fl}}) = 0, \tag{B11}$$

where the coordinate system is fixed on the sediment grains. n is porosity $\left(n = \frac{e}{1+e}\right)$, t the time, ρ_s the density of grains, ρ_f the density of fluids, q_{fl} the volume flux of the fluid relative to the solid matrix, and V is the volume of an infinitesimal element of porous material with constant sediment mass.

The fluid mass flux, can be expressed using Darcy's law:

$$\nabla\cdot(\rho_f q_{\mathrm{fl}}) = -\nabla\cdot\left(\frac{\rho_f k}{u}\nabla\cdot u_e\right), \tag{B12}$$

where μ is the viscosity of water, k the intrinsic permeability, and u_e the overpressure. The overpressure is the difference between pore fluid pressure, u and hydrostatic pore pressure u_h:

$$u_e = u - u_h. \tag{B13}$$

Changes in fluid density are related to changes in fluid pressure (Palciauskas & Domenico, 1989):

$$\frac{1}{\rho_f} d\rho_f = \beta_f du, \tag{B14}$$

where β_f is the isothermal fluid compressibility. Changes in solid density depend in a complex way on the mean stress and fluid pressure. Small changes in solid density can be linearly approximated as:

$$\frac{1-n}{\rho_s} d\rho_s = \beta_s d\sigma_m - n\beta_{s'} d, \tag{B15}$$

where β_s, $\beta_{s'}$ are solid-grain compressibilities (Palciauskas & Domenico, 1989).

Assuming that solid grains are incompressible, Equation B11, combined with Equations B12, B14, and B15, becomes:

$$\frac{D\varepsilon_v}{Dt} = \left(\beta_f \left(\frac{e}{1+e}\right)\right)\frac{Du}{Dt} - \frac{1}{\rho_f}\nabla\cdot\left(\frac{\rho_f k}{\mu}\nabla\cdot u_e\right). \tag{B16}$$

Substitution of Equation 10 into Equation B16 then yields:

$$\left(\beta_f\left(\frac{e}{1+e}\right) + \xi_m\right)\frac{Du}{Dt} = \xi_m\frac{D\sigma_m}{Dt} + \xi_q\frac{Dq}{Dt} + \frac{1}{\rho_f}\nabla\cdot\left(\frac{\rho_f k}{\mu}\nabla\cdot u_e\right). \tag{B17}$$

$$\text{With} \quad S = \beta_f\frac{e}{1+e} + \xi_m \,(\text{storage coefficient}) : \tag{B18}$$

$$\frac{Du}{Dt} = \underbrace{\frac{\xi_m}{S}\frac{D\sigma_m}{Dt}}_{Du^m/Dt} + \underbrace{\frac{\xi_q}{S}\frac{Dq}{Dt}}_{Du^q/Dt} + \underbrace{\frac{1}{S\rho_f}\nabla\cdot\left(\frac{\rho_f k}{\mu}\nabla\cdot u_e\right)}_{Du_e^{\text{diss}}/Dt}. \tag{B19}$$

Finally, using MCC, the storage coefficient, S (Equation 19) is expressed as:

$$S = \beta_f\frac{e}{1+e} + \xi_m = \beta_f\frac{e}{1+e} + \left[\left(\frac{\lambda-\kappa}{1+e}\right)\left(\frac{M^2-\eta^2}{M^2+\eta^2}\right) + \frac{\kappa}{1+e}\right]\left(\frac{1}{\sigma_m - u}\right) \tag{B20}$$

B1. Constant Stress Ratio

When the shear-stress ratio, $\eta = \eta_K$, remains constant (loading along a path with slope η in the $\sigma'_m - q$ space [Figure 2]), overpressure change can be expressed as a function of mean stress change.

The deviatoric stress can be expressed as a function of the mean effective stress:

$$q = \eta_K\sigma'_m = \eta_K(\sigma_m - u). \tag{B21}$$

Equation 16 can be re-written as:

$$S\frac{Du}{Dt} = \xi_m\frac{D\sigma_m}{Dt} + \xi_q\frac{Dq}{Dt} + \frac{1}{\rho_f}\nabla\cdot\left(\frac{\rho_f k}{\mu}\nabla\cdot u_e\right) \Longrightarrow$$

$$S\frac{Du}{Dt} = \xi_m\frac{D\sigma_m}{Dt} + \eta_K\xi_q\frac{D(\sigma_m - u)}{Dt} + \frac{1}{\rho_f}\nabla\cdot\left(\frac{\rho_f k}{\mu}\nabla\cdot u_e\right) \Longrightarrow$$

$$(S + \eta_K\xi_q)\frac{Du}{Dt} = (\xi_m + \eta_K\xi_q)\frac{D\sigma_m}{Dt} + \frac{1}{\rho_f}\nabla\cdot\left(\frac{\rho_f k}{\mu}\nabla\cdot u_e\right) \tag{B22}$$

Using $\eta = \eta_K$ in Equations B9–B20 and substituting in Equation B22:

$$\left(\beta_f \frac{e}{1+e} + \left(\frac{\lambda}{1+e}\right)\left(\frac{1}{\sigma_m - u}\right)\right)\frac{Du}{Dt} = \left(\frac{\lambda}{1+e}\right)\left(\frac{1}{\sigma_m - u}\right)\frac{D\sigma_m}{Dt} + \frac{1}{\rho_f}\nabla\cdot\left(\frac{\rho_f k}{\mu}\nabla\cdot u_e\right), \tag{B23}$$

or

$$\frac{Du}{Dt} = \frac{\xi_K}{S_K}\frac{D\sigma_m}{Dt} + \frac{1}{S_K\rho_f}\nabla\cdot\left(\frac{\rho_f k}{\mu}\nabla\cdot u_e\right), \tag{B24}$$

where ξ_K is the load efficiency coefficient for compression with a constant stress ratio:

$$\xi_K = \left(\frac{\lambda}{1+e}\right)\left(\frac{1}{\sigma_m - u}\right), \tag{B25}$$

and S_K the storage coefficient for compression with a constant stress ratio:

$$S_K = \beta_f \frac{e}{1+e} + \xi_K \tag{B26}$$

Equation B24 can be expressed as a function of vertical stress changes under certain stress conditions:

1. Under triaxial conditions, $K = \frac{\sigma'_h}{\sigma'_v}$, and $d\sigma'_m = \frac{1+2K}{3}d\sigma'_v$. Equation B24 then becomes:

$$S_K\frac{Du}{Dt} = \xi_K\frac{D\sigma'_m}{Dt} + \xi_K\frac{Du}{Dt} + \frac{1}{\rho_f}\nabla\cdot\left(\frac{\rho_f k}{\mu}\nabla\cdot u_e\right) \Longrightarrow$$

$$\left(\beta_f\frac{e}{1+e}\right)\frac{Du}{Dt} = \xi_K\frac{1+2K}{3}\frac{D\sigma'_v}{Dt} + \frac{1}{\rho_f}\nabla\cdot\left(\frac{\rho_f k}{\mu}\nabla\cdot u_e\right) \Longrightarrow$$

$$\left(\beta_f\frac{e}{1+e} + \xi_v\right)\frac{Du}{Dt} = \xi_v\frac{D\sigma_v}{Dt} + \frac{1}{\rho_f}\nabla\cdot\left(\frac{\rho_f k}{\mu}\nabla\cdot u_e\right) \Longrightarrow$$

$$\frac{Du}{Dt} = \frac{\xi_v}{S_v}\frac{D\sigma_v}{dt} + \frac{1}{S_v\rho_f}\nabla\cdot\left(\frac{\rho_f k}{\mu}\nabla\cdot u_e\right), \tag{B27}$$

   with $S_v = \beta_f\frac{e}{1+e} + \xi_v$, and $\xi_v = \xi_K\frac{1+2K}{3}$

2. For plane-strain conditions, we assume that the vertical stress remains principal, and estimate the intermediate principal stress from (Roscoe & Burland, 1968):

$$\sigma'_2 = \sigma'_3 + \left(\sigma'_1 - \sigma'_3\right)\frac{9\eta^2 + (2\eta - 3)M^2 + 18\eta}{4\eta(M^2+9)} \tag{B28}$$

   With $\Lambda = \frac{9\eta^2+(2\eta-3)M^2+18\eta}{4\eta(M^2+9)}$ and $\sigma'_3 = \sigma'_v$, $d\sigma'_m = \frac{2+(1+\Lambda)K-\Lambda}{3}d\sigma'_v$, and

$$\frac{Du}{Dt} = \frac{\xi_v}{S_v}\frac{D\sigma_v}{dt} + \frac{1}{S_v\rho_f}\nabla\cdot\left(\frac{\rho_f k}{\mu}\nabla\cdot u_e\right), \tag{B29}$$

   with $S_v = \beta_f\frac{e}{1+e} + \xi_v$, and $\xi_v = \xi_K\frac{2+(1+\Lambda)K-\Lambda}{3}$.

B2. Variation of Pore-Pressure Coefficient ξ_K/S_K in Accretionary Wedges

We show that for typical sediments in accretionary wedges, the pore-pressure coefficient ξ_K/S_K is practically independent of the initial stress state and generated overpressures are practically equal to the total mean stress change (Equation B24).

In general, overpressure generation depends on the initial stress state (σ'_m, e; Equations B24 and B26). For a given void ratio (stress states lying on the same iso-porosity; e.g., Figure 2), the mean effective stress decreases as the shear-stress ratio increases toward critical state. This decrease in the mean effective stress increases both the loading efficiency and the storage coefficients (Equations B25 and B26). Hence, initial (pre-loading) stress states with higher shear-stress ratios (e.g., close to critical state) are expected to generate more overpressure.

To explore the contribution of the initial stress state to generated overpressure for typical sediments in accretionary wedges, we consider 8 different compaction states corresponding to burial depths varying from 1 to 6 km (Table B1). We assume a friction angle of $\phi' = 25°$, $\beta_f = 5 \times 10^{-4}$ MPa^{-1}, $\kappa = 0.01$, $\lambda = 0.1$. We range the stress ratio, η_K from 0 (isotropic compaction) to 0.98 (critical state) along the iso-porosity line corresponding to each state (constant void ratio, e; Figure B1a), and calculate the mean effective stress (Equation B5). Using Equations B25 and B26, we calculate the pore-pressure coefficient ξ_K/S_K (Figure B1b). The coefficient increases with increasing shear-stress ratio and, for a given porosity, it has its maximum value at critical state. Variation in the ξ_K/S_K values for a given porosity increases as porosity decreases (deeper sediments). However, all values are above 90%, illustrating that generated overpressures are practically equal to the total mean stress change (Equation B24), and that the dependence on the initial stress state (σ'_m, e) is minimal.

Table B1
Initial Compaction States Defining Eight Iso-Porosity Lines

Isotropic compression stress $\sigma' = \sigma'_e$ (MPa)	Void ratio, e	Porosity, n	Uniaxial burial depth (km)
10	0.41	0.29	0.86
20	0.34	0.25	1.64
30	0.30	0.23	2.38
40	0.27	0.21	3.11
50	0.25	0.20	3.82
60	0.23	0.19	4.51
70	0.21	0.18	5.20
80	0.2	0.17	5.88

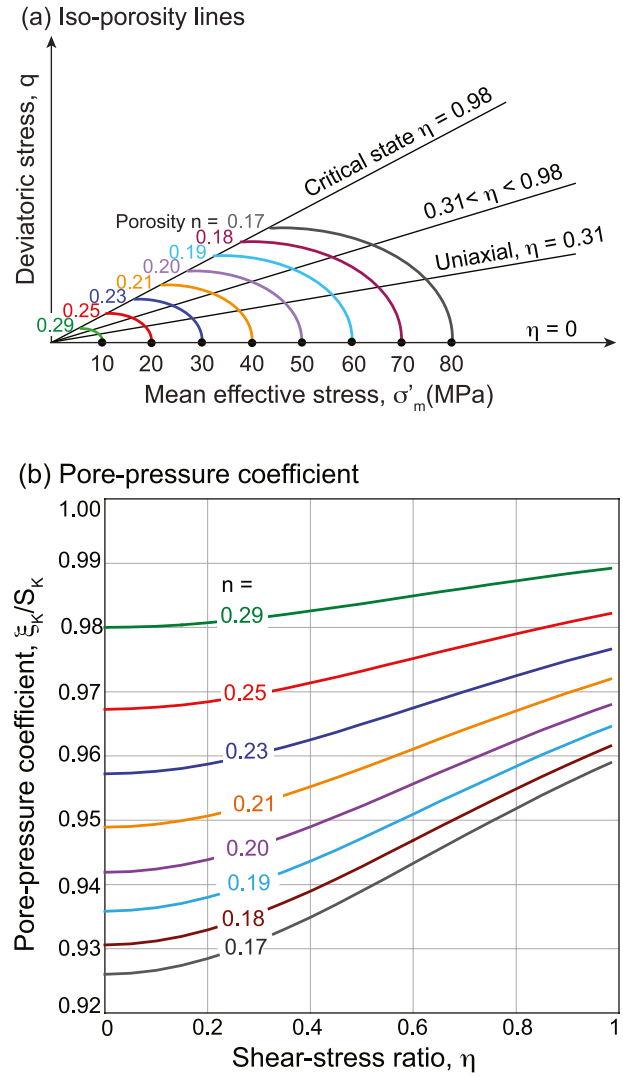

Figure B1. Contribution of initial stress state to generated overpressure for a typical wedge. (a) Iso-porosity lines corresponding to eight initial compaction states (Table B1); (b) Variation of pore pressure coefficient, $\frac{\xi_K}{S_K}$, with increasing shear-stress ratio along iso-porosity lines shown in (a).

Appendix C: Finite Element Solver and Input Parameters

C1. Finite Element Solver

We build our transient evolutionary geomechanical models in Elfen (Rockfield, 2017). Elfen is based on a finite-strain, quasistatic, finite-element formulation (Perić & Crook, 2004; Thornton et al., 2011).

The transient analyses couple deformation with stress and pore pressure by satisfying equilibrium of stresses:

$$\boldsymbol{L}^{\boldsymbol{t}}\,\boldsymbol{\sigma} + \rho_b \boldsymbol{g} = \boldsymbol{0} \tag{C1}$$

$$\boldsymbol{\sigma} = \boldsymbol{\sigma}' + u\,\boldsymbol{I} \tag{C2}$$

flow of porous fluid flow:

$$\mathrm{div}\left(\frac{k}{\mu}(\nabla u - \rho_f \boldsymbol{g})\right) = (\beta_f n + \beta_s(1-n))\frac{\partial u}{\partial t} - \frac{1}{1-n}\frac{\partial n}{\partial t} \tag{C3}$$

and constitutive laws of sediments, as described by the SR3 model (Crook, Owen, et al., 2006). A single phase of pore water is considered in the model. The code solves the mechanical equations (C1, C2, and constitutive equations) separately using a large-deformation, quasi-static, Lagrangian, explicit algorithm (Crook, Owen, et al., 2006), and the pore-fluid-flow equation (C3) using an implicit algorithm over an increment of time. Fluid flow in the seepage field is relative to the deformation of the mesh in the mechanical field. Pore pressure calculated in the seepage field is then transferred to the mechanical field using the volumetric strain at user-specified time intervals, which ensure that the difference between seepage and mechanical pore pressure remains minimal. At the end of each coupling interval, the simulation outputs pore pressure and the effective stress tensor. The total stress tensor can then be calculated using Equation C2.

C2. SR3 Input Material Properties

Table C1
SR3 Material Model Input Parameters (Crook, Owen, et al., 2006; Rockfield, 2017)

Symbol	Parameter name	Value
A	Material constant	−0.28
B	Material constant	−0.28
c	Material constant	−2
E_{ref}	Reference Young's modulus	40 MPa
$\sigma_m^{t_0}$	Initial tensile intercept (Figure C2)	−0.085 MPa
$\sigma_m^{c_0}$	Init. compressive intercept (Figure C2)	1 MPa
n_{sr3}	Material constant	1.3
n_e	Material constant	0.3
β	Friction parameter	60°
ν	Poisson's ratio	0.25
ρ_s	Grain density	2.7 g/cm^3
ρ_w	Water density	1 g/cm^3

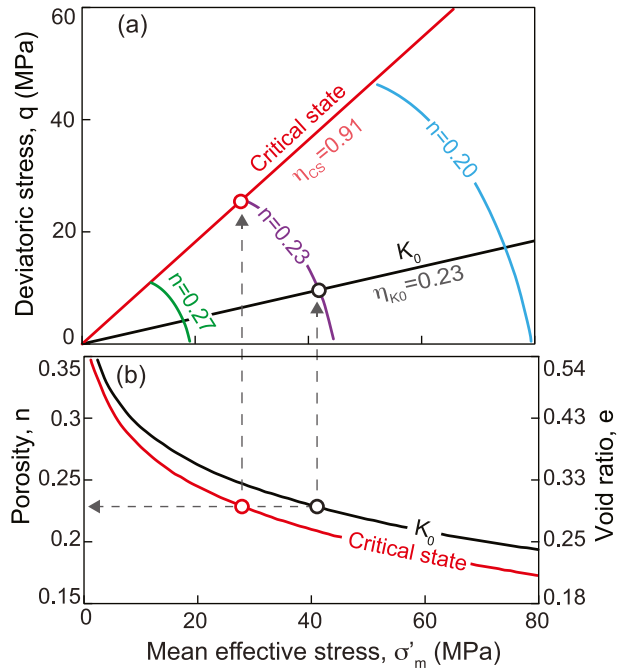

Figure C1. (Equivalent to Figure 2 for the SR3 formulation): (a) Iso-porosity lines and uniaxial compaction path in $\sigma'_m - q$ space. (b) Compaction curves under uniaxial burial (black) and critical state (red) conditions, in $\sigma'_m - n$ space.

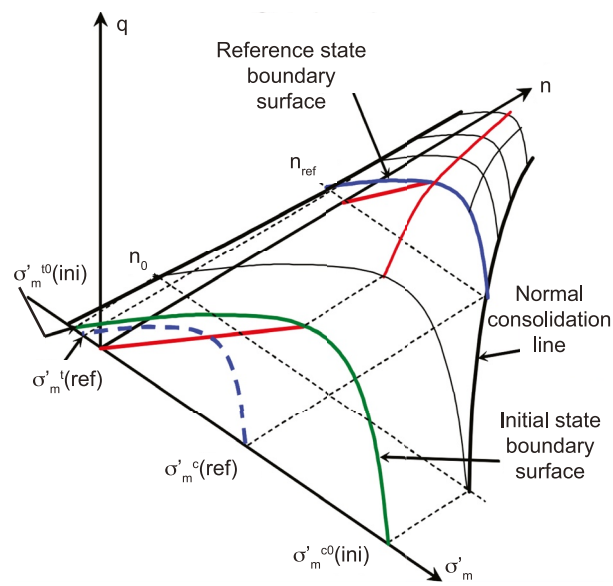

Figure C2. SR3 stress-strain-strength behavior in $\sigma'_m - q - n$ space (Rockfield, 2017).

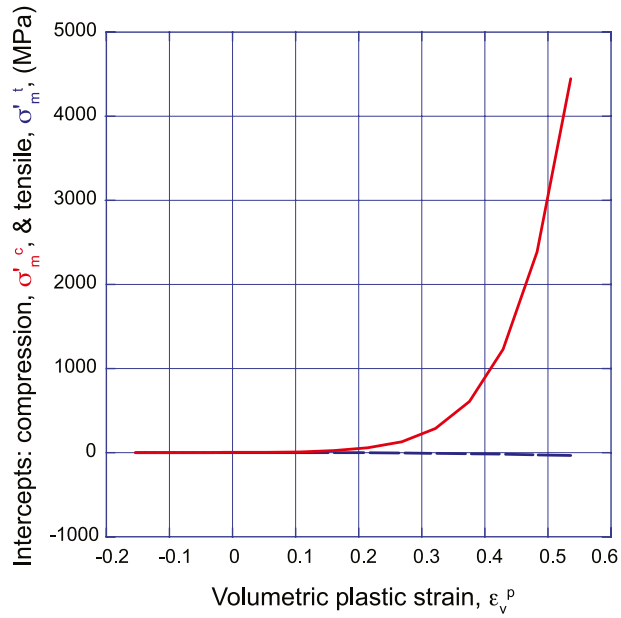

Figure C3. Hardening input for SR3 defined as a relationship between volumetric strain (ε_v^p), compression intercept, σ_m^c (solid red line), and tensile intercept, σ_m^t (dashed blue line). σ_m^c and σ_m^t are the two intercepts of the yield surface with the isotropic axis and control how the SR3 yield surface grows with applied deformation (specifically volumetric plastic strain). Negative volumetric strains and a small tensile strength are included for numerical stability (Rockfield, 2017).

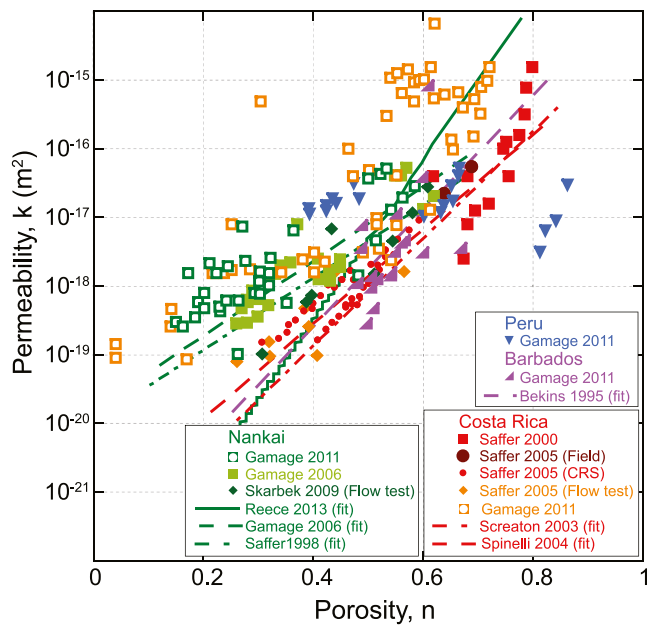

Figure C4. Published permeability-porosity field and experimental data and models for Nankai (green shades), Costa Rica (red), Barbados (purple), and Peru (blue) (Bekins et al., 1995; Gamage et al., 2011; Gamage & Screaton, 2006; Reece et al., 2013; Saffer & Bekins, 1998; Saffer et al., 2000; Saffer & McKiernan, 2005; E. J. Screaton & Saffer, 2003; Skarbek & Saffer, 2009; Spinelli et al., 2004).

Appendix D: Decomposition of Overpressure Components

We parse the individual components of Equation 18 for a loading increment t_0–t_1 (Figure D1). The effective stress path (orange line, Figure D1a) and overpressures u_{e0}, u_{e1} at the beginning and end of the increment (blue, Figure D1a) are shown.

The reduced total stress can be obtained by (green line, Figure D1):

$$\sigma_m - u_h = \sigma'_m + u_e \tag{D1}$$

where u_h is the hydrostatic pressure. The overpressure change for the increment is (blue in Figure D1a):

$$\Delta u_e = u_{e1} - u_{e0} \tag{D2}$$

If no dissipation of pore pressure were allowed (undrained conditions, Figure D1b), this overpressure change could be decomposed into a mean-stress-induced (Δu_e^m, green in Figure D1b) and a shear-induced pressure change (Δu_e^q, red in Figure D1b). With Skempton's $a = 1$, the mean-stress-induced component is:

$$\Delta u_e^m = \Delta\sigma_m = \sigma_{m1} - \sigma_{m0} \tag{D3}$$

For the hypothetical undrained scenario, the shear-induced overpressure component (Δu_e^q) is equal to the change in mean effective stress along a loading path that achieves the same change in shear stress as the actual path but does not change the volume (porosity). This path is described mathematically in the constitutive model as an

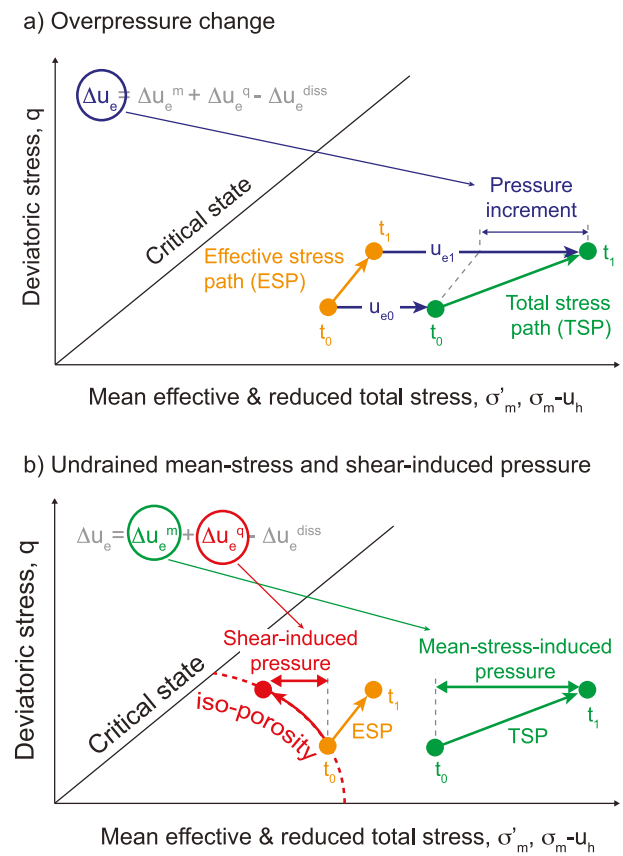

Figure D1. Schematic illustration of overpressure components for an increment in effective stress from t_0 to t_1. (a) Effective stress path (orange) as well as overpressure at the beginning and end of the increment (u_{e0}, u_{e1}, blue colors). The net overpressure change, Δu_e, is calculated as the difference between u_{e0} and u_{e1} (Equation D2). Total stresses are calculated using Equation D1 (green). (b) Assuming no dissipation (undrained conditions), the mean-stress-induced overpressure (Δu_e^m) is calculated from the total stress path (green), using Equation D3. The shear-induced overpressure (Δu_e^q) is calculated from the undrained loading path that achieves the same change in shear stress as the actual path with no volume change (iso-porosity, dashed red line).

iso-porosity curve (dashed red curve, Figure D1b). The form of this iso-porosity curve depends on the constitutive assumptions for sediment behavior. In the Critical State framework, its key attribute is that with increasing shear, a considerably decreased mean effective stress is correlated to the same porosity. Thus, under undrained conditions, increasing shear leads to an increase in overpressure (red in Figure D1b):

$$\Delta u_e^q = \sigma'_{m0} - \sigma'_{m1u} \tag{D4}$$

In practice, a significant amount of overpressure dissipates. With all other components known, pressure dissipation is calculated as:

$$\Delta u_e^{\text{diss}} = \Delta u_e^m + \Delta u_e^q - \Delta u_e \tag{D5}$$

In our model results (e.g., Figure 10c) the pressure components of Equation 18 are calculated using Equations D2–D5 and the SR3 constitutive model. However, the fundamental form of Equation 18 is independent of the exact choice of soil model, provided that the constitutive formulation describes volumetric change as a function of both mean and shear stress.

Appendix E: Effect of Convergence Rate

We explore the influence of convergence rate on pressure and stress with three models having convergence rates of 1 mm/year (slow), 5 mm/year (medium), and 10 mm/year (high) (Table 1, Models 5, 2, and 6).

We compare overpressures along the vertical profiles, "A," where the thickness of sediment above the décollement is 4 km (Figures E1a–E1c). Both overpressure and overpressure ratio, λ^*, increase with increase in convergence rate (Figures E1d and E1e). At the décollement, the overpressure increases from 15 to 22 MPa (Figure E1d), and λ^* from 0.29 to 0.43 (Figure E1e). A higher convergence rate increases the loading rate, such that the generated pressure significantly outpaces pressure dissipation.

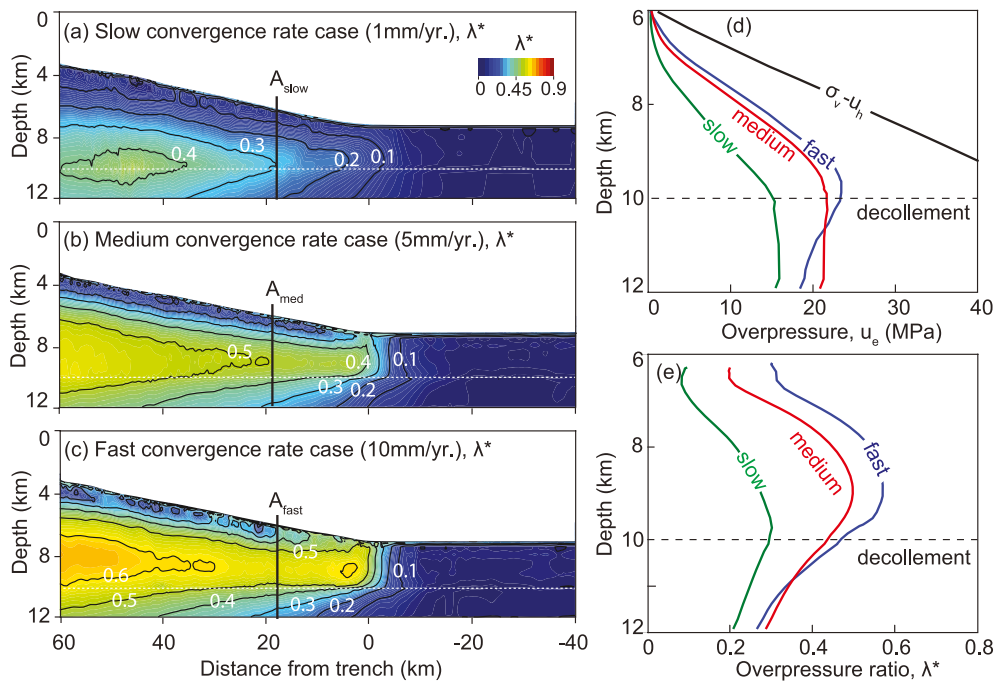

Figure E1. Impact of convergence rate on overpressure (Table 1, Models 5, 2, and 6). (a–c) Overpressure ratio (λ^*) from slow-, medium-, and fast-convergence case. The medium-convergence case is the same as the base model (Model 2, Table 1). (d) Comparison of overpressure along vertical profile A in (a–c), located where the hanging-wall thickness is 4 km. (e) Overpressure ratio (λ^*) along A profiles in (a–c). Green, red, and blue represent slow, medium, and fast convergence rates, respectively.

Increase in the convergence rate leads to decrease in both mean-effective and deviatoric stress in the hanging-wall (Figure E2d). As a result, porosity loss in the hanging-wall is less than in the slow convergence rate case (Figures E2a–E2c and E2e). Specifically, porosity offsets resulting from high and low convergence rates are 2 and 4 porosity units, respectively (Table 1, Model 5 vs. Model 6).

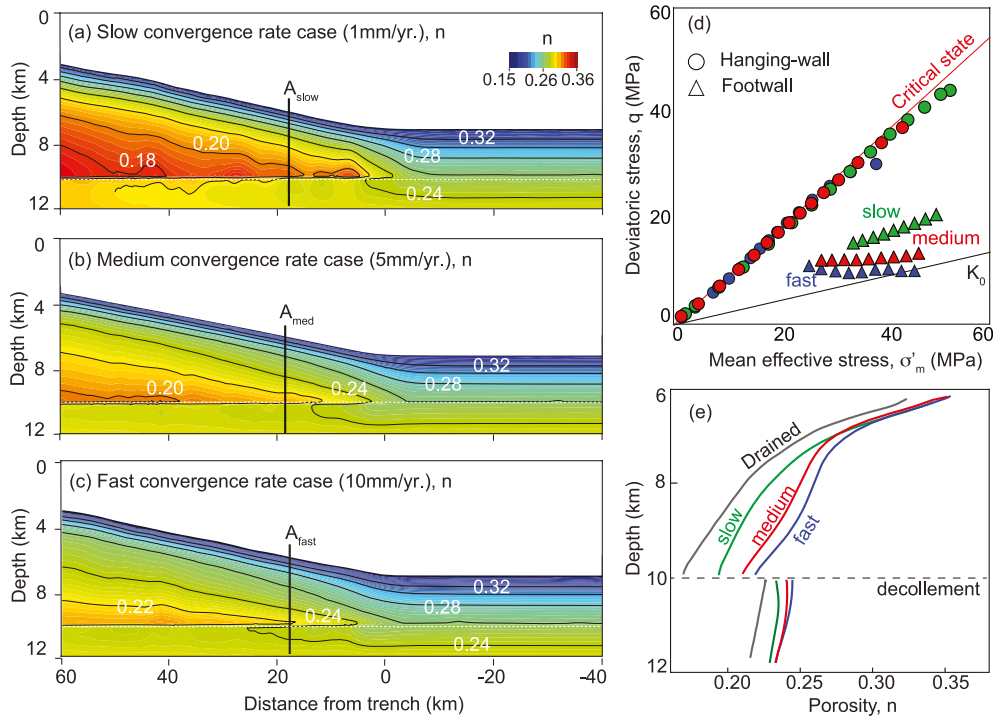

Figure E2. Impact of convergence rate on stresses and compaction. (a–c) Porosity distribution for slow-, medium-, and fast-convergence rate models. (d) Mean effective stress and deviatoric stress along vertical profiles A_{slow}, A_{med}, and A_{fast} in (a–c). Circles represent stress states in the hanging wall and triangles in footwall. (e) Porosity-depth curves along same profiles in (a–c). Green, red and blue colors represent slow, medium, and fast convergence rates, respectively. The gray line in (e) shows the drained porosity-depth curve.

Conflict of Interest

The authors declare no conflicts of interest relevant to this study.

Data Availability Statement

Elfen-project input, analysis, and output files for all models discussed in this manuscript are available on The University of Texas at Austin Dataverse Collection (https://doi.org/10.18738/T8/PZRHHO). Additionally, input data for the analyses are provided in Tables 1 and C1, and Figures 6, 7, C1, C3, and C4. The Finite Element program Elfen used in this study is a software package commercially available from Rockfield Global (Rockfield, 2017).

Acknowledgments
We thank Drs. Hiroko Kitajima and Michael Drews for their detailed and insightful reviews. This work was funded by NSF award EAR-2041496 (Nikolinakou) and the UT GeoFluids Consortium, which is currently supported by the following companies: BP, Chevron, Conoco-Phillips, ENI, Hess, Oxy, Petrobras, Shell, and Woodside. Gao was supported by USSSP during her IODP CLSI at sea program. Saffer was supported by a Jackson School of Geosciences Fellowship at The University of Texas at Austin during earlier stages of the research.

References

Albertz, M., & Sanz, P. F. (2012). Critical state finite element models of contractional fault-related folding: Part 2. Mechanical analysis. *Tectonophysics*, *576–577*, 150–170. https://doi.org/10.1016/j.tecto.2012.06.016

Angus, D. A., Dutko, M., Kristiansen, T. G., Fisher, Q. J., Kendall, J. M., Baird, A. F., et al. (2015). Integrated hydro-mechanical and seismic modelling of the Valhall reservoir: A case study of predicting subsidence, AVOA and microseismicity. *Geomechanics for Energy and the Environment*, *2*, 32–44. https://doi.org/10.1016/j.gete.2015.05.002

Araki, E., Saffer, D. M., Kopf, A. J., Wallace, L. M., Kimura, T., Machida, Y., et al. (2017). Recurring and triggered slow-slip events near the trench at the Nankai Trough subduction megathrust. *Science*, *356*(6343), 1157–1160. https://doi.org/10.1126/science.aan3120

Bangs, N. L. B., Westbrook, G. K., Ladd, J. W., & Buhl, P. (1990). Seismic velocities from the Barbados Ridge Complex: Indicators of high pore fluid pressures in an accretionary complex. *Journal of Geophysical Research*, *95*(B6), 8767–8782. https://doi.org/10.1029/jb095ib06p08767

Barnes, P. M., Ghisetti, F. C., Ellis, S., & Morgan, J. K. (2018). The role of protothrusts in frontal accretion and accommodation of plate convergence, Hikurangi subduction margin, New Zealand. *Geosphere*, *14*(2), 440–468. https://doi.org/10.1130/ges01552.1

Bekins, B. A., & Dreiss, S. (1992). A simplified analysis of parameters controlling dewatering in accretionary prisms. *Earth and Planetary Science Letters*, *109*(3–4), 275–287. https://doi.org/10.1016/0012-821x(92)90092-a

Bekins, B. A., Dreiss, S., & McCaffrey, A. M. (1995). Episodic and constant flow models for the origin of low-chloride waters in a modern accretionary complex. *Water Resources Research*, *31*(12), 3205–3215. https://doi.org/10.1029/95WR02569

Borja, R. I., & Dreiss, S. J. (1989). Numerical modeling of accretionary wedge mechanics: Application to the Barbados subduction problem. *Journal of Geophysical Research*, *94*(B7), 9323–9339. https://doi.org/10.1029/JB094iB07p09323

Bourlange, S., Henry, P., Moore, J. C., Mikada, H., & Klaus, A. (2003). Fracture porosity in the decollement zone of Nankai accretionary wedge using logging while drilling resistivity data. *Earth and Planetary Science Letters*, *209*(1–2), 103–112. https://doi.org/10.1016/S0012-821X(03)00082-7

Bray, C. J., & Karig, D. E. (1985). Porosity of sediments in accretionary prisms and some implications for dewatering processes. *Journal of Geophysical Research*, *90*(B1), 768–778. https://doi.org/10.1029/jb090ib01p00768

Brückmann, W., Moran, K., & Housen, B. (1997). Directional properties of p-wave velocities and acoustic anisotropies in different structural domains of the Northern Barbados Ridge accretionary complex. In *Paper presented at the Proceedings of the ocean drilling program: Scientific results*.

Buiter, S. J. H., Schreurs, G., Albertz, M., Gerya, T. V., Kaus, B., Landry, W., et al. (2016). Benchmarking numerical models of brittle thrust wedges. *Journal of Structural Geology*, *92*, 140–177. https://doi.org/10.1016/j.jsg.2016.03.003

Butler, J. P., Beaumont, C., & Jamieson, R. A. (2013). The Alps 1: A working geodynamic model for burial and exhumation of (ultra)high-pressure rocks in Alpine-type orogens. *Earth and Planetary Science Letters*, *377–378*, 114–131. https://doi.org/10.1016/j.epsl.2013.06.039

Byrne, T., & Fisher, D. (1990). Evidence for a weak and overpressured decollement beneath sediment-dominated accretionary prisms. *Journal of Geophysical Research*, *95*(B6), 9081–9097. https://doi.org/10.1029/jb095ib06p09081

Calahorrano, B. A., Sallares, V., Collot, J., Sage, F., & Ranero, C. (2008). Nonlinear variations of the physical properties along the southern Ecuador subduction channel: Results from depth-migrated seismic data. *Earth and Planetary Science Letters*, *267*(3–4), 453–467. https://doi.org/10.1016/j.epsl.2007.11.061

Chesley, C. J. (2022). *Marine electromagnetic studies of the Pacific Plate and Hikurangi Margin, New Zealand*. Columbia University.

Clift, P., & Vannucchi, P. (2004). Controls on tectonic accretion versus erosion in subduction zones: Implications for the origin and recycling of the continental crust. *Reviews of Geophysics*, *42*(2), RG2001. https://doi.org/10.1029/2003rg000127

Costa Pisani, P., Reshef, M., & Moore, G. (2005). Targeted 3-D prestack depth imaging at Legs 190-196 ODP drill sites (Nankai Trough, Japan). *Geophysical Research Letters*, *32*(20), n/a. https://doi.org/10.1029/2005GL024191

Craig, R. F. (2005). *Soil mechanics* (7th ed.). Spon Press.

Crook, A. J. L., Owen, D. R. J., Willson, S. M., & Yu, J. G. (2006). Benchmarks for the evolution of shear localisation with large relative sliding in frictional materials. *Computer Methods in Applied Mechanics and Engineering*, *195*(37–40), 4991–5010. https://doi.org/10.1016/j.cma.2005.11.016

Crook, A. J. L., Willson, S. M., Yu, J. G., & Owen, D. R. J. (2006). Predictive modelling of structure evolution in sandbox experiments. *Journal of Structural Geology*, *28*(5), 729–744. https://doi.org/10.1016/j.jsg.2006.02.002

Dahlen, F. A., Suppe, J., & Davis, D. (1984). Mechanics of fold-and-thrust belts and accretionary wedges; cohesive Coulomb theory. *Journal of Geophysical Research*, *89*(B12), 10087–10101. https://doi.org/10.1029/jb089ib12p10087

Davis, D., Suppe, J., & Dahlen, F. A. (1983). Mechanics of fold-and-thrust belts and accretionary wedges. *Journal of Geophysical Research*, *88*(B2), 1153–1172. https://doi.org/10.1029/JB088iB02p01153

Davis, E. E., Hyndman, R. D., & Villinger, H. (1990). Rates of fluid expulsion across the Northern Cascadia Accretionary Prism: Constraints from new heat row and multichannel seismic reflection data. *Journal of Geophysical Research*, *95*(B6), 8869. https://doi.org/10.1029/JB095iB06p08869

Drews, M. C., & Duschl, F. (2022). Overpressure, vertical stress, compaction and horizontal loading along the North Alpine Thrust Front, SE Germany. *Marine and Petroleum Geology*, *143*, 105806. https://doi.org/10.1016/j.marpetgeo.2022.105806

Ellis, S., Fagereng, Å., Barker, D., Henrys, S., Saffer, D., Wallace, L., et al. (2015). Fluid budgets along the northern Hikurangi subduction margin, New Zealand: The effect of a subducting seamount on fluid pressure. *Geophysical Journal International*, *202*(1), 277–297. https://doi.org/10.1093/gji/ggv127

Ellis, S., Ghisetti, F., Barnes, P. M., Boulton, C., Fagereng, Å., & Buiter, S. (2019). The contemporary force balance in a wide accretionary wedge: Numerical models of the southcentral Hikurangi margin of New Zealand. *Geophysical Journal International*, *219*(2), 776–795. https://doi.org/10.1093/gji/ggz317

Flemings, P. B. (2021). *A concise guide to geopressure: Origin, prediction, and applications*. Cambridge Press.

Flemings, P. B., Long, H., Dugan, B., Germaine, J. T., John, C. M., Behrmann, J. H., et al. (2008). Pore pressure penetrometers document high overpressure near the seafloor where multiple submarine landslides have occurred on the continental slope, offshore Louisiana, Gulf of Mexico. *Earth and Planetary Science Letters*, *269*(3–4), 309–325. https://doi.org/10.1016/j.epsl.2007.12.005

Flemings, P. B., & Saffer, D. M. (2018). Pressure and stress prediction in the Nankai accretionary prism: A critical state soil mechanics porosity-based approach. *Journal of Geophysical Research: Solid Earth*, *123*(2), 1089–1115. https://doi.org/10.1002/2017jb015025

French, M. E., & Morgan, J. K. (2020). Pore fluid pressures and strength contrasts maintain frontal fault activity, Northern Hikurangi Margin, New Zealand. *Geophysical Research Letters*, *47*(21), e2020GL089209. https://doi.org/10.1029/2020gl089209

Gamage, K., & Screaton, E. (2006). Characterization of excess pore pressures at the toe of the Nankai accretionary complex, Ocean Drilling Program sites 1173, 1174, and 808: Results of one-dimensional modeling. *Journal of Geophysical Research*, *111*(B4), B04103. https://doi.org/10.1029/2004jb003572

Gamage, K., Screaton, E., Bekins, B., & Aiello, I. (2011). Permeability–porosity relationships of subduction zone sediments. *Marine Geology*, *279*(1–4), 19–36. https://doi.org/10.1016/j.margeo.2010.10.010

Gao, B., Flemings, P. B., Nikolinakou, M. A., Saffer, D. M., & Heidari, M. (2018). Mechanics of fold-and-thrust belts based on geomechanical modeling. *Journal of Geophysical Research: Solid Earth*, *123*(5), 4454–4474. https://doi.org/10.1029/2018JB015434

Ge, S., & Screaton, E. (2005). Modeling seismically induced deformation and fluid flow in the Nankai subduction zone. *Geophysical Research Letters*, *32*(17), L17301. https://doi.org/10.1029/2005gl023473

Gradmann, S., & Beaumont, C. (2017). Numerical modelling study of mechanisms of mid-basin salt canopy evolution and their potential applications to the Northwestern Gulf of Mexico. *Basin Research*, *29*(4), 490–520. https://doi.org/10.1111/bre.12186

Hamahashi, M., Saito, S., Kimura, G., Yamaguchi, A., Fukuchi, R., Kameda, J., et al. (2013). Contrasts in physical properties between the hanging wall and footwall of an exhumed seismogenic megasplay fault in a subduction zone-An example from the Nobeoka Thrust Drilling Project. *Geochemistry, Geophysics, Geosystems*, *14*(12), 5354–5370. https://doi.org/10.1002/2013gc004818

Hauser, M. R., Couzens-Schultz, B. A., & Chan, A. W. (2014). Estimating the influence of stress state on compaction behavior. *Geophysics*, *79*(6), D389–D398. https://doi.org/10.1190/geo2014-0089.1

Heidari, M., Nikolinakou, M. A., Hudec, M. R., & Flemings, P. B. (2019). Influence of a reservoir bed on diapirism and drilling hazards near a salt diapir: A geomechanical approach. *Petroleum Geoscience*, *25*(3), 282–297. https://doi.org/10.1144/petgeo2018-113

Henry, P., Jouniaux, L., Screaton, E. J., Hunze, S., & Saffer, D. M. (2003). Anisotropy of electrical conductivity record of initial strain at the toe of the Nankai accretionary wedge. *Journal of Geophysical Research*, *108*(B9), n/a. https://doi.org/10.1029/2002JB002287

Henry, P., & Wang, C.-Y. (1991). Modeling of fluid flow and pore pressure at the toe of Oregon and Barbados Accretionary Wedges. *Journal of Geophysical Research*, *96*(B12), 20109–20130. https://doi.org/10.1029/91jb01908

Housen, B. A., Tobin, H. J., Labaume, P., Leitch, E. C., & Maltman, A. J. (1996). Strain decoupling across the decollement of the Barbados accretionary prism. *Geology*, *24*(2), 127–130. https://doi.org/10.1130/0091-7613(1996)024<0127:sdatdo>2.3.co;2

Hubbert, M. K., & Rubey, W. W. (1959). Role of fluid pressure in mechanics of overthrust faulting Part I. Mechanics of fluid-filled porous solids and its application to overthrust faulting. *Geological Society of America Bulletin*, *70*(2), 115–166. https://doi.org/10.1130/0016-7606(1959)70[115:rofpim]2.0.co;2

Ikari, M. J., & Saffer, D. M. (2011). Comparison of frictional strength and velocity dependence between fault zones in the Nankai accretionary complex. *Geochemistry, Geophysics, Geosystems*, *12*(4), n/a. https://doi.org/10.1029/2010GC003442

Ikari, M. J., Saffer, D. M., & Marone, C. (2009). Frictional and hydrologic properties of a major splay fault system, Nankai subduction zone. *Geophysical Research Letters*, *36*(20), L20313. https://doi.org/10.1029/2009gl040009

Im, K., Saffer, D., Marone, C., & Avouac, J.-P. (2020). Slip-rate-dependent friction as a universal mechanism for slow slip events. *Nature Geoscience*, *13*(10), 705–710. https://doi.org/10.1038/s41561-020-0627-9

Ito, Y., & Obara, K. (2006). Dynamic deformation of the accretionary prism excites very low frequency earthquakes. *Geophysical Research Letters*, *33*(2), L02311. https://doi.org/10.1029/2005gl025270

Karig, D. E. (1986). Physical properties and mechanical state of accreted sediments in the Nankai Trough, Southwest Japan Arc. *Geological Society of America Memoirs*, *166*, 117–134.

Karig, D. E. (1990). Experimental and observational constraints on the mechanical behaviour in the toes of accretionary prisms. In R. J. Knipe & E. H. Rutter (Eds.), *Deformation mechanisms, rheology, and tectonics*, *Geological Society Special Publication* (Vol. 54, pp. 383–398). Geological Society of London.

Karig, D. E. (1993). Reconsolidation tests and sonic velocity measurements of clay-rich sediments from the Nankai Trough. In I. A. Hill, A. Taira, & J. V. Firth (Eds.), *Proceedings of the ocean drilling program, scientific results, Leg 131* (Vol. 131, pp. 247–260). Ocean Drilling Program.

Kitajima, H., Saffer, D., Sone, H., Tobin, H., & Hirose, T. (2017). In situ stress and pore pressure in the deep interior of the Nankai accretionary prism, integrated ocean drilling program site C0002. *Geophysical Research Letters*, *44*(19), 9644–9652. https://doi.org/10.1002/2017gl075127

Kitajima, H., & Saffer, D. M. (2012). Elevated pore pressure and anomalously low stress in regions of low frequency earthquakes along the Nankai Trough subduction megathrust. *Geophysical Research Letters*, *39*(23), L23301. https://doi.org/10.1029/2012gl053793

Kodaira, S., Iidaka, T., Kato, A., Park, J. O., Iwasaki, T., & Kaneda, Y. (2004). High pore fluid pressure may cause silent slip in the Nankai Trough. *Science*, *304*(5675), 1295–1298. https://doi.org/10.1126/science.1096535

Kodaira, S., No, T., Nakamura, Y., Fujiwara, T., Kaiho, Y., Miura, S., et al. (2012). Coseismic fault rupture at the trench axis during the 2011 Tohoku-oki earthquake. *Nature Geoscience*, *5*(9), 646–650. https://doi.org/10.1038/ngeo1547

Kopf, A., & Brown, K. M. (2003). Friction experiments on saturated sediments and their implications for the stress state of the Nankai and Barbados subduction thrusts. *Marine Geology*, *202*(3–4), 193–210. https://doi.org/10.1016/s0025-3227(03)00286-x

Kozdon, J. E., & Dunham, E. M. (2013). Rupture to the trench: Dynamic rupture simulations of the 11 March 2011 Tohoku earthquake. *Bulletin of the Seismological Society of America*, *103*(2B), 1275–1289. https://doi.org/10.1785/0120120136

Liu, Y., & Rice, J. R. (2007). Spontaneous and triggered aseismic deformation transients in a subduction fault model. *Journal of Geophysical Research*, *112*(B9), B09404. https://doi.org/10.1029/2007JB004930

Mannu, U., Ueda, K., Willett, S. D., Gerya, T. V., & Strasser, M. (2016). Impact of sedimentation on evolution of accretionary wedges: Insights from high-resolution thermomechanical modeling. *Tectonics*, *35*(12), 2828–2846. https://doi.org/10.1002/2016tc004239

Moore, J. C., & Saffer, D. (2001). Updip limit of the seismogenic zone beneath the accretionary prism of southwest Japan: An effect of diagenetic to low-grade metamorphic processes and increasing effective stress. *Geology*, *29*(2), 183–186. https://doi.org/10.1130/0091-7613(2001)029<0183:ulotsz>2.0.co;2

Morgan, J. K. (2015). Effects of cohesion on the structural and mechanical evolution of fold and thrust belts and contractional wedges: Discrete element simulations. *Journal of Geophysical Research: Solid Earth*, *120*(5), 3870–3896. https://doi.org/10.1002/2014jb011455

Morgan, J. K., Karig, D. E., & Maniatty, A. (1994). The estimation of diffuse strains in the toe of the western Nankai accretionary prism: A kinematic solution. *Journal of Geophysical Research*, *99*(B4), 7019–7032. https://doi.org/10.1029/93jb03367

Neuzil, C. E. (1995). Abnormal pressures as hydrodynamic phenomena. *American Journal of Science*, *295*(6), 742–786. https://doi.org/10.2475/ajs.295.6.742

Nikolinakou, M. A., Flemings, P. B., Heidari, M., & Hudec, M. R. (2018). Stress and pore pressure in mudrocks bounding salt systems. *Rock Mechanics and Rock Engineering*, *51*(12), 3883–3894. https://doi.org/10.1007/s00603-018-1540-z

Nollet, S., Kleine Vennekate, G. J., Giese, S., Vrolijk, P., Urai, J. L., & Ziegler, M. (2012). Localization patterns in sandbox-scale numerical experiments above a normal fault in basement. *Journal of Structural Geology*, *39*, 199–209. https://doi.org/10.1016/j.jsg.2012.02.011

Nolting, A., Zahm, C. K., Kerans, C., & Nikolinakou, M. A. (2018). Effect of carbonate platform morphology on syndepositional deformation: Insights from numerical modeling. *Journal of Structural Geology*, *115*, 91–102. https://doi.org/10.1016/j.jsg.2018.07.003

Obana, K., & Kodaira, S. (2009). Low-frequency tremors associated with reverse faults in a shallow accretionary prism. *Earth and Planetary Science Letters*, *287*(1–2), 168–174. https://doi.org/10.1016/j.epsl.2009.08.005

Obradors-Prats, J., Rouainia, M., Aplin, A. C., & Crook, A. J. L. (2017). Hydromechanical modeling of stress, pore pressure, and porosity evolution in fold-and-thrust belt systems. *Journal of Geophysical Research: Solid Earth*, *122*(11), 9383–9403. https://doi.org/10.1002/2017jb014074

Owens, W. H. (1993). Magnetic fabric studies of samples from Hole 808C, Nankai Trough. In *Paper presented at the Proc. ODP Sci. Res.*

Palciauskas, V. V., & Domenico, P. A. (1989). Fluid pressures in deforming porous rocks. *Water Resources Research*, *25*(2), 203–213. https://doi.org/10.1029/wr025i002p00203

Park, J.-O., Fujie, G., Wijerathne, L., Hori, T., Kodaira, S., Fukao, Y., et al. (2010). A low-velocity zone with weak reflectivity along the Nankai subduction zone. *Geology*, *38*(3), 283–286. https://doi.org/10.1130/g30205.1

Party, O. D. P. L. S. (1987). Expulsion of fluids from depth along a subduction-zone decollement horizon. *Nature*, *326*(6115), 785–788. https://doi.org/10.1038/326785a0

Perić, D., & Crook, A. J. L. (2004). Computational strategies for predictive geology with reference to salt tectonics. *Computer Methods in Applied Mechanics and Engineering*, *193*(48–51), 5195–5222. https://doi.org/10.1016/j.cma.2004.01.037

Reece, J. S., Flemings, P. B., & Germaine, J. T. (2013). Data report: Permeability, compressibility, and microstructure of resedimented mudstone from IODP Expedition 322, site C0011. In S. Saito, M. B. Underwood, Y. Kubo, & the Expedition 322 Scientists (Eds.), *Expedition 322, site C0011, IODP Proceedings*. IODP.

Rockfield. (2017). *ELFEN forward modeling user manual*. Rockfield Software Limited.

Roscoe, K. H., & Burland, J. B. (1968). On the generalized stress-strain behaviour of "wet" clay. In J. Heyman & F. A. Leckie (Eds.), *Engineering plasticity* (pp. 535–609). Cambridge University Press.

Roscoe, K. H., Schofield, A. N., & Wroth, C. P. (1958). On the yielding of soils. *Géotechnique*, *8*(1), 22–53. https://doi.org/10.1680/geot.1958.8.1.22

Rowe, K. T., Screaton, E. J., & Ge, S. (2012). Coupled fluid flow and deformation modeling of the frontal thrust region of the Kumano Basin transect, Japan: Implications for fluid pressures and decollement downstepping. *Geochemistry, Geophysics, Geosystems*, *13*(3), 1–18. Q0ad23. https://doi.org/10.1029/2011gc003861

Ruh, J. B., Sallarès, V., Ranero, C. R., & Gerya, T. (2016). Crustal deformation dynamics and stress evolution during seamount subduction: High-resolution 3-D numerical modeling. *Journal of Geophysical Research: Solid Earth*, *121*(9), 6880–6902. https://doi.org/10.1002/2016jb013250

Saffer, D. M. (2015). The permeability of active subduction plate boundary faults. *Geofluids*, *15*(1–2), 193–215. https://doi.org/10.1111/gfl.12103

Saffer, D. M., & Bekins, B. A. (1998). Episodic fluid flow in the Nankai accretionary complex: Timescale, geochemistry, flow rates and fluid budget. *Journal of Geophysical Research*, *103*(B12), 30351–30370. https://doi.org/10.1029/98jb01983

Saffer, D. M., & Bekins, B. A. (2006). An evaluation of factors influencing pore pressure in accretionary complexes: Implications for taper angle and wedge mechanics. *Journal of Geophysical Research*, *111*(B04101), B04101. https://doi.org/10.1029/2005JB003990

Saffer, D. M., & McKiernan, A. W. (2005). Permeability of underthrust sediments at the Costa Rican subduction zone: Scale dependence and implications for dewatering. *Geophysical Research Letters*, *32*(2), L02302. https://doi.org/10.1029/2004gl021388

Saffer, D. M., Silver, E. A., Fisher, A. T., Tobin, H., & Moran, K. (2000). Inferred pore pressures at the Costa Rica subduction zone: Implications for dewatering processes. *Earth and Planetary Science Letters*, *177*(3–4), 193–207. https://doi.org/10.1016/s0012-821x(00)00048-0

Saffer, D. M., & Tobin, H. J. (2011). Hydrogeology and mechanics of subduction zone forearcs: Fluid flow and pore pressure. *Annual Review of Earth and Planetary Sciences*, *39*(1), 157–186. https://doi.org/10.1146/annurev-earth-040610-133408

Schneider, J., Flemings, P. B., Dugan, B., Long, H., & Germaine, J. T. (2009). Overpressure and consolidation near the seafloor of Brazos-Trinity Basin IV, northwest deepwater Gulf of Mexico. *Journal of Geophysical Research: Solid Earth*, *114*(B5), B05102. https://doi.org/10.1029/2008jb005922

Scholz, C. H. (1998). Earthquakes and friction laws. *Nature*, *391*(6662), 37–42. https://doi.org/10.1038/34097

Scholz, C. H. (2012). *The mechanics of earthquakes and faulting*. Cambridge University Press.

Screaton, E., Carson, B., Davis, E., & Becker, K. (2000). Permeability of a decollement zone: Results from a two-well experiment in the Barbados accretionary complex. *Journal of Geophysical Research*, *105*(B9), 21403–21410. https://doi.org/10.1029/2000JB900220

Screaton, E., Saffer, D., Henry, P., & Hunze, S. (2002). Porosity loss within the underthrust sediments of the Nankai accretionary complex: Implications for overpressures. *Geology*, *30*(1), 19–22. https://doi.org/10.1130/0091-7613(2002)030<0019:Plwtus>2.0.Co;2

Screaton, E. J., & Saffer, D. M. (2003). Numerical modeling of dewatering of underthrust sediments, Costa Rica Subduction Zone. *Eos, Transactions American Geophysical Union*, *84*(46). Paper presented at the Eos Trans. AGU Fall Meet. Suppl., Abstract T52C-0275.

Shi, Y., Wang, C.-Y., Hwang, W.-T., & von Huene, R. (1989). Hydrogeological modeling of porous flow in the Oregon accretionary prism. *Geology*, *17*(4), 321–323. https://doi.org/10.1130/0091-7613(1989)017<0321:hmopfi>2.3.co;2

Skarbek, R. M., & Saffer, D. M. (2009). Pore pressure development beneath the décollement at the Nankai subduction zone: Implications for plate boundary fault strength and sediment dewatering. *Journal of Geophysical Research*, *114*(B7), B07401. https://doi.org/10.1029/2008JB006205

Skempton, A. W. (1954). The pore-pressure coefficients A and B. *Géotechnique*, *4*(4), 143–147. https://doi.org/10.1680/geot.1954.4.4.143

Song, I., Saffer, D. M., & Flemings, P. B. (2011). Mechanical characterization of slope sediments: Constraints on in situ stress and pore pressure near the tip of the megasplay fault in the Nankai accretionary complex. *Geochemistry, Geophysics, Geosystems*, *12*(8), Q0AD17. https://doi.org/10.1029/2011gc003556

Spinelli, G., Saffer, D. M., & Underwood, M. B. (2004). Effects of along-strike variability in temperature and diagenetic fluid sources on fluid flow patterns in the Nicoya Margin Subduction Zone, Costa Rica. *Eos, Transactions American Geophysical Union*, *85*(28). Paper presented at the Eos Trans. AGU, West. Pac. Geophys. Meet. Suppl., Abstract T22A-04.

Spitz, R., Bauville, A., Epard, J.-L., Kaus, B. J. P., Popov, A. A., & Schmalholz, S. M. (2020). Control of 3-D tectonic inheritance on fold-and-thrust belts: Insights from 3-D numerical models and application to the Helvetic nappe system. *Solid Earth*, *11*(3), 999–1026. https://doi.org/10.5194/se-11-999-2020

Stauffer, P., & Bekins, B. A. (2001). Modeling consolidation and dewatering near the toe of the northern Barbados accretionary complex. *Journal of Geophysical Research*, *106*(B4), 6369–6383. https://doi.org/10.1029/2000jb900368

Suess, E., Bohrmann, G., von Huene, R., Linke, P., Wallmann, K., Lammers, S., et al. (1998). Fluid venting in the eastern Aleutian Subduction Zone. *Journal of Geophysical Research*, *103*(B2), 2597–2614. https://doi.org/10.1029/97jb02131

Sugioka, H., Okamoto, T., Nakamura, T., Ishihara, Y., Ito, A., Obana, K., et al. (2012). Tsunamigenic potential of the shallow subduction plate boundary inferred from slow seismic slip. *Nature Geoscience*, *5*(6), 414–418. https://doi.org/10.1038/ngeo1466

Sun, T., Ellis, S., & Saffer, D. (2020). Coupled evolution of deformation, pore fluid pressure, and fluid flow in shallow subduction forearcs. *Journal of Geophysical Research: Solid Earth*, *125*(3), e2019JB019101. https://doi.org/10.1029/2019jb019101

Suppe, J. (2007). Absolute fault and crustal strength from wedge tapers. *Geology*, *35*(12), 1127. https://doi.org/10.1130/g24053a.1

Suppe, J. (2014). Fluid overpressures and strength of the sedimentary upper crust. *Journal of Structural Geology*, *69*, 481–492. https://doi.org/10.1016/j.jsg.2014.07.009

Terzaghi, K. (1925). *Erdbaumechanik auf Bodenphysikalischer Grundlage*. F. Deuticke.

Terzaghi, K., Peck, R. B., & Mesri, G. (1996). *Soil mechanics in engineering practice* (3rd ed.). Wiley.

Thigpen, J. R., Roberts, D., Snow, J. K., Walker, C. D., & Bere, A. (2019). Integrating kinematic restoration and forward finite element simulations to constrain the evolution of salt diapirism and overburden deformation in evaporite basins. *Journal of Structural Geology*, *118*, 68–86. https://doi.org/10.1016/j.jsg.2018.10.003

Thornton, D. A., & Crook, A. J. L. (2014). Predictive modeling of the evolution of fault structure: 3-D modeling and coupled geomechanical/flow simulation. *Rock Mechanics and Rock Engineering*, *47*(5), 1533–1549. https://doi.org/10.1007/s00603-014-0589-6

Thornton, D. A., Roberts, D. T., Crook, A. J. L., & Yu, J. G. (2011). Regional scale salt tectonics modelling: Bench-scale validation and extension to field-scale predictions. In *Paper presented at the beyond balanced sections: Geological Society of America Conference, Minneapolis, MN*.

Tobin, H. J., & Saffer, D. M. (2009). Elevated fluid pressure and extreme mechanical weakness of a plate boundary thrust, Nankai Trough subduction zone. *Geology*, *37*(8), 679–682. https://doi.org/10.1130/G25752a.1

Tsuji, T., Tokuyama, H., Costa Pisani, P., & Moore, G. (2008). Effective stress and pore pressure in the Nankai accretionary prism off the Muroto Peninsula, southwestern Japan. *Journal of Geophysical Research*, *113*(B11), B11401. https://doi.org/10.1029/2007jb005002

Wallace, L. M., Kaneko, Y., Hreinsdóttir, S., Hamling, I., Peng, Z., Bartlow, N., et al. (2017). Large-scale dynamic triggering of shallow slow slip enhanced by overlying sedimentary wedge. *Nature Geoscience*, *10*(10), 765–770. https://doi.org/10.1038/ngeo3021

Wang, C. Y., Hwang, W. T., & Cochrane, G. R. (1994). Tectonic dewatering and mechanics of protothrust zones: Example from the Cascadia accretionary margin. *Journal of Geophysical Research*, *99*(B10), 20043–20050. https://doi.org/10.1029/94jb01545

Wang, H. (2000). *Theory of linear poroelasticity: With applications to geomechanics and hydrogeology*. Princeton University Press.

Wang, K. L., & Hu, Y. (2006). Accretionary prisms in subduction earthquake cycles: The theory of dynamic Coulomb wedge. *Journal of Geophysical Research: Solid Earth*, *111*(B6), B06410. https://doi.org/10.1029/2005jb004094

Wood, D. M. (1990). *Soil behaviour and critical state soil mechanics*. Cambridge University Press.

Yamano, M., Foucher, J. P., Kinoshita, M., Fisher, A., & Hyndman, R. D. (1992). Heat flow and fluid flow regime in the western Nankai accretionary prism. *Earth and Planetary Science Letters*, *109*(3–4), 451–462. https://doi.org/10.1016/0012-821x(92)90105-5

Yuan, T., Spence, G., & Hyndman, R. (1994). Seismic velocities and inferred porosities in the accretionary wedge sediments at the Cascadia margin. *Journal of Geophysical Research*, *99*(B3), 4413–4427. https://doi.org/10.1029/93jb03203

Zhang, J., Hüpers, A., Kreiter, S., & Kopf, A. J. (2021). Pore pressure regime and fluid flow processes in the shallow Nankai trough subduction zone based on experimental and modeling results from IODP site C0023. *Journal of Geophysical Research: Solid Earth*, *126*(2), e2020JB020248. https://doi.org/10.1029/2020jb020248